AFRL-AFOSR-VA-TR-2024-0028

Integrated Multi-Physics, Multi-scale Computational Modeling Framework for Multifunctional Applications

Ghosh, Somnath
JOHNS HOPKINS UNIV BALTIMORE MD
3400 NORTH CHARLES STREET
BALTIMORE, MD,
US

11/12/2023
Final Technical Report

Air Force Research Laboratory
Air Force Office of Scientific Research
Arlington, Virginia 22203
Air Force Materiel Command

REPORT DOCUMENTATION PAGE

PLEASE DO NOT RETURN YOUR FORM TO THE ABOVE ORGANIZATION.

1. REPORT DATE	2. REPORT TYPE	3. DATES COVERED	
20231112	Final	START DATE 20180901	END DATE 20230531

4. TITLE AND SUBTITLE
Integrated Multi-Physics, Multi-scale Computational Modeling Framework for Multifunctional Applications

5a. CONTRACT NUMBER	5b. GRANT NUMBER	5c. PROGRAM ELEMENT NUMBER
	FA9550-18-1-0536	61102F

5d. PROJECT NUMBER	5e. TASK NUMBER	5f. WORK UNIT NUMBER

6. AUTHOR(S)
Somnath Ghosh

7. PERFORMING ORGANIZATION NAME(S) AND ADDRESS(ES)
JOHNS HOPKINS UNIV BALTIMORE MD
3400 NORTH CHARLES STREET
BALTIMORE, MD
US

8. PERFORMING ORGANIZATION REPORT NUMBER

9. SPONSORING/MONITORING AGENCY NAME(S) AND ADDRESS(ES)	10. SPONSOR/MONITOR'S ACRONYM(S)	11. SPONSOR/MONITOR'S REPORT NUMBER(S)
Air Force Office of Scientific Research 875 N. Randolph St. Room 3112 Arlington, VA 22203	AFRL/AFOSR RTB2	AFRL-AFOSR-VA-TR-2024-0028

12. DISTRIBUTION/AVAILABILITY STATEMENT
A Distribution Unlimited: PB Public Release

13. SUPPLEMENTARY NOTES

14. ABSTRACT
Multifunctional systems are gaining importance in Air Force applications like small UAVs, conformal load?bearing antenna, health monitoring damage sensors, stretchable electronics etc. They are constituted of heterogeneous materials, e.g., piezoelectric materials, organized in hybrid architectures at different scales of hierarchy. Rigorous multiscale, multi?physics analyses can help with material design for enhancing the multi?functionality. However, there is a lack of models and codes with comprehensive predictive capabilities. The proposed research has developed an integrated, multi?scale modeling system coupling electrical fields with finite deformation and material damage evolution. It has incorporated spatial multi?scaling for realizing the effect of microstructure and material degradation on multi?physics response functions. The overall objective of this research is to develop a multiscale virtual damage sensor for piezoelectric composite materials through correlation functions between electrical, deformation and damage fields.

15. SUBJECT TERMS

16. SECURITY CLASSIFICATION OF:			17. LIMITATION OF ABSTRACT	18. NUMBER OF PAGES
a. REPORT	b. ABSTRACT	c. THIS PAGE		
U	U	U	UU	2

19a. NAME OF RESPONSIBLE PERSON	19b. PHONE NUMBER *(Include area code)*
BYUNG LEE	426-8483

Standard Form 298 (Rev.5/2020)
Prescribed by ANSI Std. Z39.18

REPORT DOCUMENTATION PAGE

Form Approved
OMB No. 0704-0188

1. REPORT DATE *(DD-MM-YYYY)*	2. REPORT TYPE	3. DATES COVERED *(From - To)*
08/05/2023	FINAL PERFORMANCE REPORT	09/01/2018- 05/30/2023

4. TITLE AND SUBTITLE
Integrated Multi-Physics, Multi-scale Computational Modeling Framework for Multifunctional Applications

5a. CONTRACT NUMBER

5b. GRANT NUMBER
FA9550-18-1-0536

5c. PROGRAM ELEMENT NUMBER

6. AUTHOR(S)

Somnath Ghosh
Professor, Department of Civil & Systems Engineering,
Mechanical Engineering, and Materials Science & Engineering
Johns Hopkins University, Baltimore, MD 21218

5d. PROJECT NUMBER

5e. TASK NUMBER

5f. WORK UNIT NUMBER

7. PERFORMING ORGANIZATION NAME(S) AND ADDRESS(ES)
JOHNS HOPKINS UNIVERSITY
Department of Civil & Systems Engineering
201F Latrobe, 3400 N. Charles Street, Baltimore, MD 21218

8. PERFORMING ORGANIZATION REPORT NUMBER

9. SPONSORING/MONITORING AGENCY NAME(S) AND ADDRESS(ES)
Air Force Office of Scientific Research (AFOSR)
Program: Mechanics of Multifunctional Materials & Microsystems

10. SPONSOR/MONITOR'S ACRONYM(S)
Program Manager:
Dr. B.L. Lee

11. SPONSOR/MONITOR'S REPORT NUMBER(S)

12. DISTRIBUTION/AVAILABILITY STATEMENT

Approved for public release

13. SUPPLEMENTARY NOTES

14. ABSTRACT

The overall objective was to develop a multiscale virtual damage sensor for piezoelectric composite materials through correlation functions between electrical, deformation and damage fields. Major accomplishments include: (i) Image-based microstructure reconstruction and characterization using 2-point correlation functions and PCA; (ii) Unified finite deformation phase field model for modeling crack propagation in piezocomposite microstructures; (iii) Wavelet enriched adaptive hierarchical framework; (iv) Calibration and representation of the macroscopic damage parameters in terms of microstructural morphology in PUCDM; and (v) Correlating surface electrical signals to subsurface damage fields.

15. SUBJECT TERMS

Multi-scale, multi-physics analyses; electrical field; finite deformation; damage evolution; virtual damage sensor; piezoelectric composite; image based microstructure; unified finite deformation phase field model for crack propagation; wavelet enriched adaptive hierarchy; parametrically upscaled continuum damage model;

16. SECURITY CLASSIFICATION OF:			17. LIMITATION OF ABSTRACT	18. NUMBER OF PAGES	19a. NAME OF RESPONSIBLE PERSON
a. REPORT	b. ABSTRACT	c. THIS PAGE			Somnath Ghosh
					19b. TELEPHONE NUMBER *(Include area code)*
unclassified	unclassified	unclassified		65	(410) 516 7833

INSTRUCTIONS FOR COMPLETING SF 298

1. REPORT DATE. Full publication date, including day, month, if available. Must cite at least the year and be Year 2000 compliant, e.g. 30-06-1998; xx-06-1998; xx-xx-1998.

2. REPORT TYPE. State the type of report, such as final, technical, interim, memorandum, master's thesis, progress, quarterly, research, special, group study, etc.

3. DATE COVERED. Indicate the time during which the work was performed and the report was written, e.g., Jun 1997 - Jun 1998; 1-10 Jun 1996; May - Nov 1998; Nov 1998.

4. TITLE. Enter title and subtitle with volume number and part number, if applicable. On classified documents, enter the title classification in parentheses.

5a. CONTRACT NUMBER. Enter all contract numbers as they appear in the report, e.g. F33315-86-C-5169.

5b. GRANT NUMBER. Enter all grant numbers as they appear in the report. e.g. AFOSR-82-1234.

5c. PROGRAM ELEMENT NUMBER. Enter all program element numbers as they appear in the report, e.g. 61101A.

5e. TASK NUMBER. Enter all task numbers as they appear in the report, e.g. 05; RF0330201; T4112.

5f. WORK UNIT NUMBER. Enter all work unit numbers as they appear in the report, e.g. 001; AFAPL30480105.

6. AUTHOR(S). Enter name(s) of person(s) responsible for writing the report, performing the research, or credited with the content of the report. The form of entry is the last name, first name, middle initial, and additional qualifiers separated by commas, e.g. Smith, Richard, J, Jr.

7. PERFORMING ORGANIZATION NAME(S) AND ADDRESS(ES). Self-explanatory.

8. PERFORMING ORGANIZATION REPORT NUMBER. Enter all unique alphanumeric report numbers assigned by the performing organization, e.g. BRL-1234; AFWL-TR-85-4017-Vol-21-PT-2.

9. SPONSORING/MONITORING AGENCY NAME(S) AND ADDRESS(ES). Enter the name and address of the organization(s) financially responsible for and monitoring the work.

10. SPONSOR/MONITOR'S ACRONYM(S). Enter, if available, e.g. BRL, ARDEC, NADC.

11. SPONSOR/MONITOR'S REPORT NUMBER(S). Enter report number as assigned by the sponsoring/ monitoring agency, if available, e.g. BRL-TR-829; -215.

12. DISTRIBUTION/AVAILABILITY STATEMENT. Use agency-mandated availability statements to indicate the public availability or distribution limitations of the report. If additional limitations/ restrictions or special markings are indicated, follow agency authorization procedures, e.g. RD/FRD, PROPIN, ITAR, etc. Include copyright information.

13. SUPPLEMENTARY NOTES. Enter information not included elsewhere such as: prepared in cooperation with; translation of; report supersedes; old edition number, etc.

14. ABSTRACT. A brief (approximately 200 words) factual summary of the most significant information.

15. SUBJECT TERMS. Key words or phrases identifying major concepts in the report.

16. SECURITY CLASSIFICATION. Enter security classification in accordance with security classification regulations, e.g. U, C, S, etc. If this form contains classified information, stamp classification level on the top and bottom of this page.

17. LIMITATION OF ABSTRACT. This block must be completed to assign a distribution limitation to the abstract. Enter UU (Unclassified Unlimited) or SAR (Same as Report). An entry in this block is necessary if the abstract is to be limited.

Integrated Multi-Physics, Multi-scale Computational Modeling Framework for Multifunctional Applications

Sponsor: Air Force Office of Scientific Research,
Mechanics of Multifunctional Materials & Microsystems

Grant No. FA9550-18-1-0536

Period of Performance: September 1, 2018- May 30, 2023

Program Directors: Dr. Byung "Les" Lee

Principal Investigator
Somnath Ghosh
Professor, Department of Civil & Systems Engineering,
Mechanical Engineering, and Materials Science & Engineering
Johns Hopkins University, Baltimore, MD 21218

August 5, 2023

Acknowledgments

The author would like to thank the Air Force Office of Scientific Research, Mechanics of Multi-functional Materials & Microsystems Program for providing sponsorship of this work. The author is especially thankful to the program director Dr. B.-L. (Les) Lee for his continued support and insights. Computational support for this work has been provided by the the Advanced Research Computing at Hopkins (ARCH) core facility supported by the National Science Foundation (NSF) grant number OAC 1920103. Computational support of this work is also provided by an AFOSR DURIP grant FA9550-21-1-0303, for which the program director is Dr. B.-L. (Les) Lee. The views and conclusions contained herein are those of the authors only and should not be interpreted as representing those of AFOSR or the U.S. Government.

Contents

List of Figures

List of Tables

Abstract

Multifunctional systems are gaining importance in Air Force applications like small UAVs, conformal load-bearing antenna, health monitoring damage sensors, stretchable electronics etc. They are constituted of heterogeneous materials, e.g. piezoelectric materials, organized in hybrid architectures at different scales of hierarchy. Rigorous multi-scale, multi-physics analyses can help with material design for enhancing the multi-functionality. However, there is a lack of models and codes with comprehensive predictive capabilities. The proposed research has developed an integrated, multi-scale modeling system coupling electrical fields with finite deformation and material damage evolution. It has incorporated spatial multi-scaling for realizing the effect of microstructure and material degradation on multi-physics response functions. The overall objective of this research is to develop a multiscale virtual damage sensor for piezoelectric composite materials through correlation functions between electrical, deformation and damage fields. Two major tasks towards this goal are: (i) Hierarchical multi-scaling with parametric upscaling to build effective, structure-scale material response functions from multi-physics simulations at lower scales; and (ii) Virtual damage sensing using a top-down connection with piezoelectric materials through correlation functions between surface electric field and subsurface damage.

Major accomplishments that have achieved in this research thus far are:

- Image based microstructure reconstruction and characterization using 2-point correlation functions and Principal Component Analysis(PCA)
- Unified finite deformation phase field model for modeling crack propagation in piezocomposites microstructures
- Wavelet enriched adaptive hierarchical framework to alleviate the computational costs associated with phase field problems
- Calibration and representation of the macroscopic damage parameters in terms of microstructural morphology
- Correlating surface electrical signals to subsurface damage fields

An important advancement in this research is the establishment of a coupled electromechanical finite deformation phase field model for crack propagation and interfacial decohesion in multiphase piezoelectric composites with interfaces. The crack phase field model is augmented with cohesive traction-separation laws at the material interfaces, derived from a cohesive potential function. A Gibbs free energy density function is proposed, allowing for the incorporation of the anisotropic

elastic stiffness of the piezoelectric material. Numerical simulations exhibiting different failure mechanisms are carried out to demonstrate the efficacy of the model. Effects of external electric field on crack evolution and the competition between penetration and deflection of a crack impinging on an interface are investigated. Limited verification tests are conducted with theoretical results. Finally, the model is used to simulate fracture in nonuniform piezocomposite microstructures. The effect of crack propagation on the evolution of the electric field with different crack face conditions are analyzed. Differences in the electromechanical responses of piezocomposites due to different fiber distributions are also observed. This model is subsequently parametrically upscaled to build effective, structure-scale material response functions from multi-physics simulations at lower scales. Virtual damage sensing using a top-down connection with piezoelectric materials through correlation functions between surface electric field and subsurface damage.

Chapter 1

Relevant Information

1.1 Personnel Supported

1. Somnath Ghosh, PI
2. Saikat Dan, Ph.D. student, 100% (Will Graduate in Fall 2023)
3. Preetam Tarafder, Ph.D. student, 100% (Will Graduate in Fall 2023)

1.2 Ph.D. Dissertation Titles (tentative)

1. S. Dan, A Machine Learning-Aided Digital Twin for Damage Sensing based on a Multiphysics-Multiscale Computational Modeling Framework using Piezoelectric Composites, Johns Hopkins University, Baltimore, MD, (in progress)
2. P. Tarafder, Parametrically Upscaled Constitutive-Damage Models (PUCCDMs) Coupling Electric, Deformation and Damage Fields for Piezoelectric Composites, Johns Hopkins University, Baltimore, MD, (in progress)

1.3 Refereed Journal Publications Acknowledging this Grant

1. P. Tarafder, S. Dan and S. Ghosh, "Cohesive zone phase field model for electromechanical fracture in nonuniform piezoelectric composites", Journal of Composite Materials, Vol. 57, No. 4, 531-543, 2023.
https://doi.org/10.1177/00219983231151396.
2. S. Dan, P. Tarafder, and S. Ghosh, "Adaptive wavelet-enhanced cohesive zone phase-field FE Model for crack evolution in piezoelectric composites", Computer Methods in Applied Mechanics and Engineering, Vol. 392, Art. 114636, March 2022.
https://doi.org/10.1016/j.cma.2022.114636

3. P. Tarafder, S. Dan and S. Ghosh, "Finite deformation cohesive zone phase field model for crack propagation in multi-phase microstructures", Computational Mechanics, Vol. 66, No. 3, pp. 723-743, 2020.
https://doi.org/10.1007/s00466-020-01874-6

4. R. Yaghmaie and S. Ghosh, "Multi-time scale-based modeling of piezoelectric materials coupling transient electrical and dynamic fields with finite deformation damage", International Journal of Solids and Structures, Vol. 202, pp. 338-355, 2020.
https://doi.org/10.1016/j.ijsolstr.2020.04.033

5. S. Ghosh and S. Guo, "Developing a virtual damage sensor using a coupled electro-mechanical FE model of a piezoelectric material", International Journal for Multiscale Computational Engineering, Vol. 17, No. 4, pp. 447–468, 2019.
https://doi.org/10.1615/IntJMultCompEng.2019030797

1.4 Keynote Lectures by PI Acknowledging this Grant

1. **S. Ghosh**, Preetam Tarafder and Saikat Dan, "Towards a Virtual Damage Sensor: Using a Multiscale Coupled Electro-Mechanical FE Model of Piezoelectric Material", TMS 2020 Annual Meeting & Exhibition, San Diego, CA, February 23-27, 2020.

1.5 Invited Presentations at Conferences Acknowledging this Grant

1. **S. Ghosh**, P. Tarafder, S. Dan, "Multiscale Modeling and Machine Learning-Enabled Digital Twin for Piezocomposite Damage Sensing", TMS ICME 2023 7th World Congress, May 21–25, 2023, Orlando, Florida.

2. P. Tarafder, S. Dan and S. Ghosh, "A Machine Learning Aided Digital Twin for Damage Sensing based on a Multiphysics-Multiscale Computational Modeling Framework using Piezoelectric Composites", Poster, Data-Driven and Computational Modeling Across Scales, California Nano Systems Institute, UCLA, May 10-12, 2023.

3. S. Dan, P. Tarafder and S. Ghosh, "A Machine Learning-Aided Digital Twin for Damage Sensing based on a Multiphysics-Multiscale Computational Modeling Framework using Piezoelectric Composites", Engineering Mechanics Institute Conference 2023 (EMI 2023) ASCE, Georgia Institute of Technology, GA, June 6-9, 2023.

4. S. Dan and S. Ghosh, "Adaptive Wavelet-Enhanced Cohesive Zone Phase-Field FE Model for Crack Evolution in Piezoelectric Composites", 10th International Conference on Multiscale Materials Modeling (MMM10), Baltimore MD, October 3, 2022.

5. S. Ghosh, S. Dan and P. Tarafder, "Integrated Multi-Physics, Multi-scale Computational Modeling Framework for Multifunctional Applications", CIMTEC 2022 - 15th International Conference on Modern Materials and Technologies, Perugia, Italy, June 20-29, 2022. (Virtual)

6. S. Dan, P. Tarafder and S. Ghosh, "Adaptive Wavelet-Enhanced Cohesive Zone Phase-Field FE Model for Crack Evolution in Piezoelectric Composites", Engineering Mechanics Institute Conference, Johns Hopkins University, Baltimore, MD, June 1-3, 2022.
7. P. Tarafder, S. Dan and S. Ghosh, "Parametrically Upscaled Coupled Constitutive Model (PUCCM) for Nonuniform Unidirectional Multifunctional Composites from Micromechanical Analysis", Engineering Mechanics Institute Conference, Johns Hopkins University, Baltimore, MD, June 1-3, 2022.
8. P. Tarafder, S. Dan and S. Ghosh, "An adaptive hierarchical FE framework for crack propagation in piezocomposite microstructures using a cohesive zone phase field model", Engineering Mechanics Institute Conference, Virtual Conference, May, 2021.
9. S. Dan, P. Tarafder, and S. Ghosh, "An arc-length stabilized adaptive wavelet-enriched hierarchical finite element method for crack propagation using phase field models", US National Congress of Computational Mechanics, Virtual Meeting, July 27, 2021.
10. S. Dan, P. Tarafder and S. Ghosh, "A Computational Damage Sensor Using Electromechanically Coupled Piezoelectric Materials", 15th US National Congress of Computational Mechanics, Austin TX, July 28-August 1, 2019.

1.6 PI Awards and Accolades in this Period

1. S. Ghosh, *Distinguished Scientist/Engineer Award*, Materials Processing & Manufacturing Division, The Minerals, Metals, and Materials Society (TMS), 2023
2. S. Ghosh, *Raymond D. Mindlin Medal*, American Society of Civil Engineers (ASCE), 2022
3. S. Ghosh, *J. Tinsley Oden Medal*, US Association for Computational Mechanics (USACM), 2021
4. S. Ghosh, *Fellow*, The Minerals, Metals and Materials Society (TMS), 2021
5. S. Ghosh, *Computational Mechanics Award*, International Association for Computational Mechanics (IACM), 2020
6. S. Ghosh, *Ted Belytschko Applied Mechanics Award*, ASME Applied Mechanics Division (ASME/AMD), 2019
7. S. Ghosh, *Fellow*, Society of Engineering Science (SES) , 2019

1.7 Student Awards and Accolades in this Period

1. P. Tarafder, *1st Place Award, Student Poster Competition in Advanced Manufacturing, Materials, and Multiscale Method*, 2023 UN National Congress of Computational Mechanics, Albuquerque, NM, July 2023

2. S. Dan, *1st Place Award, Student Paper Competition in Computational Mechanics*, 2023 Engineering Mechanics Institute Conference, June 2023, Georgia Institute of Technology, Atlanta, GA

3. S. Dan, *2nd Place Award, IOP sponsored Student Poster Competition*, International Conference on Multiscale Materials Modeling (MMM 2022), Baltimore

4. S. Dan, *1st Place Award, Student Paper Competition in in Modeling Inelasticity & Multiscale Behavior*, 2022 Engineering Mechanics Institute Conference, Johns Hopkins University, Baltimore, MD. June 2022

5. P. Tarafder, *1st Place Award, Student Paper Competition in Computational Mechanics*, 2022 Engineering Mechanics Institute Conference, Johns Hopkins University, Baltimore, MD. June 2022

6. P. Tarafder, *2nd Place Award, Student Paper Competition in Modeling Inelasticity & Multiscale Behavior*, 2021 Engineering Mechanics Institute Conference, Columbia University, New York, NY, June 2021

Chapter 2

Introduction

Aerospace structures, built with composite materials, are susceptible to life-limiting catastrophes with the evolution of damage and failure under extreme loading conditions such as impact or fatigue. Microstructural damage initiates in the form of fiber-matrix interfacial debonding, fiber breakage, and matrix cracking grows across scales to manifest as mesoscopic damage in the form of inter-ply delamination leading to macroscopically unstable crack propagation and causing structural failure. For optimal reliability and survivability, preventing structural and functional failure, it is necessary for composite structures to be designed and fabricated with the capability of autonomous detection of progressing subsurface damage and consequently mitigating its progression. This objective, while daunting, can be addressed through systematic utilization of material multi functionality, coupling mechanical and electrical fields. Multifunctional structure-material systems are increasingly being used in the aerospace industry in a variety of applications like components of small unmanned airborne vehicles (UAVs), aircraft active skins, morphing wing structures, devices for vibration and noise suppression, sensors for diagnosing material degradation and responding to external stimuli, strain-mediated antenna systems, among others. These systems are typically constituted of a hybrid of piezo-electric, ferroelectric, ferromagnetic, or magneto-dielectric materials arranged in different scales of material hierarchy. Multifunctional composites not only provide lightweight, load-bearing structures, but also perform additional functions like structural health monitoring, thermal and/or electrical conductivity/storage, impact resistance, acoustic damping, self-healing, and morphing or shape-changing. Engineering these systems is becoming easier with the advent of modern manufacturing processes like 3D printing and additive manufacturing, along with novel material concepts.

The overall objective of this research is to develop a multiscale virtual damage sensor for piezoelectric composite materials through correlation functions between electrical, deformation and damage fields. An important step towards this objective is the establishment of a coupled electromechanical finite deformation phase field model for crack propagation and interfacial decohesion in multiphase piezoelectric composites with interfaces. The crack phase field model is augmented with cohesive traction-separation laws at the material interfaces, derived from a cohesive potential function. A Gibbs free energy density function is proposed, allowing for the incorporation of the anisotropic elastic stiffness of the piezoelectric material. Numerical simulations exhibiting different failure

mechanisms are carried out to demonstrate the efficacy of the model. Effects of external electric field on crack evolution and the competition between penetration and deflection of a crack impinging on an interface are investigated. Limited verification tests are conducted with theoretical results. Finally, the model is used to simulate fracture in nonuniform piezocomposite microstructures. The effect of crack propagation on the evolution of the electric field with different crack face conditions are analyzed. Differences in the electromechanical responses of piezocomposites due to different fiber distributions are also observed. This model is subsequently parametrically upscaled to build effective, structure-scale material response functions from multi-physics simulations at lower scales. Virtual damage sensing using a top-down connection with piezoelectric materials through correlation functions between surface electric field and subsurface damage.

Piezoelectric composites or piezocomposites are a special class of multiphase multifunctional materials that are widely used for engineering applications, which require strong electromechanical coupling capabilities such as sensing and actuation. They are generally developed by embedding active piezoelectric inclusions (fibers or particles) in a matrix of passive epoxy polymer. Piezocomposites provide better electromechanical coupling along with load bearing functionalities in comparison to monolithic piezoelectric ceramics. However, owing to their heterogeneous microstructures, these composites are often vulnerable to different types of failure such as interfacial debonding, and primary and secondary phase cracking [46, 48]. The design and reliable manufacture of the piezocomposites requires a proper understanding of different failure processes that influences their overall multifunctional capabilities. As such, there is a need for physics-based computational models that can be used for robust simulations of these processes to provide guidance on better design approaches.

Interfacial cracking in multiphase piezocomposites have been studied since the early nineties [56]. Theoretical analysis of the decohesion between piezoelectric inclusions and matrix, and cracks in piezoelectric bi-materials with different electrical crack face boundary conditions have been reported in literature. Issues concerning the competition between crack deflection at the interface and penetration into the interface between piezoelectric materials have been investigated for different electromechanical loading conditions [14, 16, 43–45, 64]. Many researchers have also proposed different computational models and techniques such as cohesive zone model (CZM) [23], extended finite element method (XFEM) [52], boundary element method [6] and isogeometric methods [7] for simulating interfacial cracks in piezoelectric materials. In the recent years, phase-field models for fracture problems have gained major attention due to its thermodynamically-consistent formulation that can track complex crack paths without any *a-priori* knowledge of the cracks [34, 50]. These models have been successfully used for simulating electromechanical fracture in piezoelectric and ferroelectric ceramics [2, 35, 55, 65, 66] as well as piezoelectric composites [13].

This paper builds on the cohesive zone enhanced phase-field framework developed for electromechanical fracture in piezocomposites undergoing finite deformation [13]. A stored elastic energy density function for anisotropic multiphase piezoelectric materials with interfaces is adopted such that it can be readily split into a tensile and compressive parts. The effect of the direction of external electric field on the development of crack path in piezoelectric material with interface is studied using the proposed phase field model. The competition between penetration and deflection of a crack impinging on an interface of a piezoelectric bi-material is investigated. Different failure mechanisms in piezocomposite microstructures, such as interfacial debonding, crack kinking and

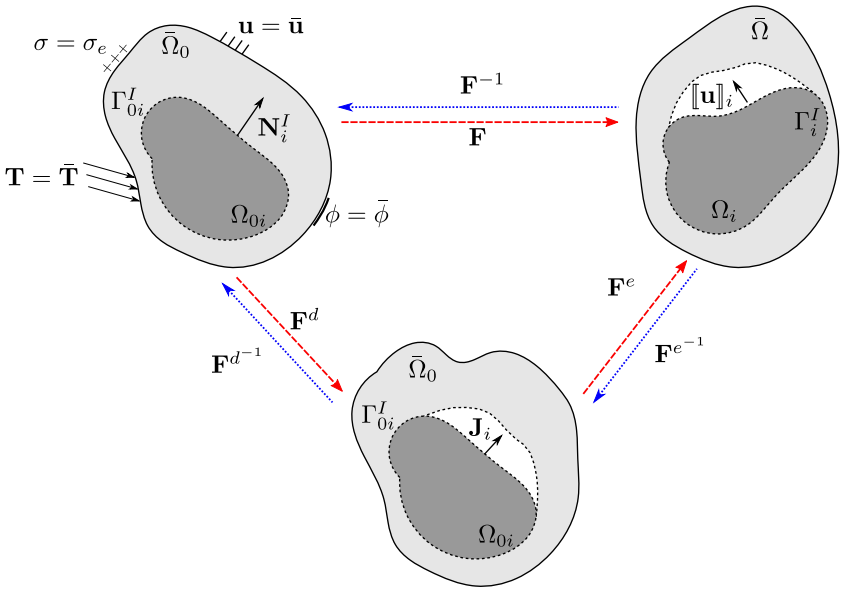

Figure 2.1: Reference (undeformed), intermediate and current configurations of a multi-phase domain subjected to electromechanical loading. The intermediate configuration is obtained through an inverse mapping of the current configuration by $\mathbf{F}^{e^{-1}}$.

propagation into the matrix, are also simulated. Comparison studies are undertaken for analyzing the differences in the evolution of electric fields with different electrical crack face conditions, as well as the influence of the distribution of inclusions on the electromechanical response.

2.1 Cohesive zone phase-field formulation for electromechanical fracture

A cohesive zone enhanced phase-field framework that has been developed for simulating crack evolution and interfacial decohesion in piezocomposites [13] is summarized in this section. The finite deformation kinematics of interfacial decohesion, regularization of sharp cracks and interfaces, and the governing equations for the coupled problem are briefly discussed in the following subsections.

2.1.1 Finite deformation kinematics of debonding across interfaces

Consider a multi-phase domain Ω with an external boundary Γ_0, containing n second-phase inclusions denoted by $\Omega_i, i = 1,\ldots,n$. The domain is subjected to electromechanical loading resulting in finite deformation as shown in Figure 2.1. $\Gamma^I_i, i = 1,\ldots,n$ denotes the internal interface of each inclusion and $\bar{\Omega} = \Omega - \cup^n_{i=1}\Omega_i$ denotes the primary matrix. The corresponding undeformed (reference) configuration of the multi-phase domain, external boundary, inclusions, internal interfaces and primary matrix are denoted by Ω_0, Γ_0, Ω_{0i}, Γ^I_{0i} and $\bar{\Omega}_0$ respectively. $\mathbf{N}^I_i$ denotes the outward normal to the interface Γ^I_{0i} pointing towards $\bar{\Omega}_0$.

Deformation of the multifunctional composite leads to debonding between the inclusion and the

primary matrix phases at the interface, resulting in a discontinuity in the displacement and electric potential fields across the interface. Accordingly, the total displacement and electric potential fields can be written as [13, 60]:

$$\mathbf{u}(\mathbf{X}) = \underbrace{\mathbf{u}^c(\mathbf{X})}_{\text{continuous}} + \underbrace{\sum_{i=1}^{n} [\![\mathbf{u}]\!]_i \mathscr{H}_{\Gamma^I_{0i}}(\mathbf{X})}_{\text{discontinuous}} \tag{2.1a}$$

$$\phi(X) = \underbrace{\phi^c(\mathbf{X})}_{\text{continuous}} + \underbrace{\sum_{i=1}^{n} [\![\phi]\!]_i \mathscr{H}_{\Gamma^I_{0i}}(\mathbf{X})}_{\text{discontinuous}} \tag{2.1b}$$

where $[\![\mathbf{u}]\!]_i$ and $[\![\phi]\!]_i$ denote the jump in the displacement and electric potential fields respectively across the i^{th} interface and $\mathscr{H}_{\Gamma^I_{0i}}(\mathbf{X})$ represents the Heaviside function. The total deformation gradient can be multiplicatively decomposed into elastic and decohesion components as:

$$\mathbf{F} = \mathbf{F}^e\mathbf{F}^d = (\mathbf{I} + \boldsymbol{\nabla}_{\mathbf{X}}\mathbf{u}^c)\left(\mathbf{I} + \sum_{i=1}^{n} \mathbf{J}_i \otimes \mathbf{N}^I_i \delta_{\Gamma^I_{0i}}\right) \tag{2.2}$$

where $\boldsymbol{\nabla}_{\mathbf{X}}$ is the gradient operator expressed in the reference configuration, $\mathbf{J}_i$ is the pull-back vector of the jump in the displacement field $[\![\mathbf{u}]\!]_i$ to the intermediate configuration given by $\mathbf{J}_i = \mathbf{F}^{e^{-1}}[\![\mathbf{u}]\!]_i$, $\delta_{\Gamma^I_{0i}}$ denotes the Dirac-delta function at the interface Γ^I_{0i} and $\otimes$ indicates the tensor product operator.

2.1.2 Phase-field regularization of sharp cracks, interfaces and field discontinuities at interfaces

In the phase-field formulation, an order parameter $s \in (0,1)$ is introduced to represent the regularized crack topology, as shown in Figure 2.2. The discrete sharp crack surface is approximated using the following functional [34, 38]:

$$\begin{aligned} \Gamma_{l_c}(s, \boldsymbol{\nabla}_{\mathbf{X}} s) &= \int_{\Omega_0} \gamma_{l_c} \, \mathrm{d}\Omega_0 \\ &= \int_{\Omega_0} \frac{1}{2l_c}\left(s^2 + l_c^2 \boldsymbol{\nabla}_{\mathbf{X}} s \cdot \boldsymbol{\nabla}_{\mathbf{X}} s\right) \mathrm{d}\Omega_0 \end{aligned} \tag{2.3}$$

where l_c is the length-scale parameter used to regularize the sharp cracks.

Implementing the cohesive zone model for interfacial decohesion requires *a-priori* knowledge of the interfacial topology. Consequently, this work adopts a regularized representation of the pre-damaged interfaces through a functional Γ_{l_l} in the undeformed configuration [38, 60]. Similar to

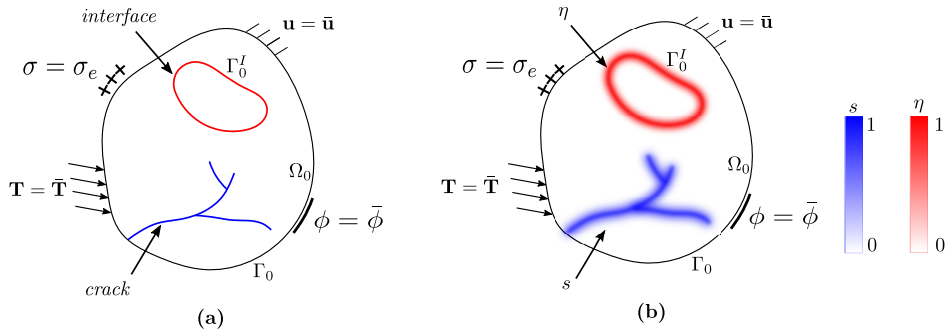

Figure 2.2: Schematic diagram of a domain containing interacting cracks and interfaces: (a) discrete representation of sharp cracks and interfaces, and (b) regularized representation of sharp cracks and interfaces.

the crack phase field order parameter s, an auxiliary interface phase field order parameter $\eta \in (0,1)$ is introduced, which represents the known interface topology in the reference configuration Ω_0. The interface order parameter $\eta(\mathbf{X})$ is evaluated by solving the equation:

$$\eta - l_I^2 \nabla_{\mathbf{X}} \cdot \nabla_{\mathbf{X}} \eta = 0 \qquad \text{in } \Omega_0 \tag{2.4}$$

subject to the Dirichlet boundary condition $\eta = 1$ on the internal interfaces $\Gamma_{0i}^I \; \forall i = 1, \ldots, n$. Here l_I is the length-scale parameter used to regularize the sharp interface topology. Moreover, the initial interface topology does not evolve with deformation. Therefore, the phase field order parameter η is solved only once before the deformation commences. With a known η field, the functional Γ_{l_I} determining the spread of the regularized interfaces can be expressed as:

$$\begin{aligned} \Gamma_{l_I}(\eta, \nabla_{\mathbf{X}}\eta) &= \int_{\Omega_0} \gamma_{l_I} \, \mathrm{d}\Omega_0 \\ &= \int_{\Omega_0} \frac{1}{2 l_I} \left(\eta^2 + l_I^2 \nabla_{\mathbf{X}} \eta \cdot \nabla_{\mathbf{X}} \eta \right) \mathrm{d}\Omega_0 \end{aligned} \tag{2.5}$$

The jump in the displacement and potential fields in Equation (2.1) at the interfaces are also approximated using the first order Taylor expansion and given as[13]:

$$[\![\mathbf{u}]\!] \approx h \nabla_{\mathbf{X}} \mathbf{u} \mathbf{N}_i^I \tag{2.6a}$$

$$[\![\phi]\!] \approx h \nabla_{\mathbf{X}} \phi \mathbf{N}_i^I \tag{2.6b}$$

where h is a small scalar field jump regularization parameter. The normal $\mathbf{N}_i^I$ to the interface Γ_{0i}^I is evaluated from the interface phase field order parameter η as:

$$\mathbf{N}_i^I = \frac{\nabla_{\mathbf{X}} \eta}{\| \nabla_{\mathbf{X}} \eta \|} |_{\mathbf{X} \in \Gamma_{0i}^I} \tag{2.7}$$

where $\|\cdot\|$ corresponds to the L_2 norm of a vector.

To incorporate the interfacial decohesion in the phase-field framework, the deformation gradient tensor $\mathbf{F}^d$ in Equation (2.2) is expressed in terms of the regularized interface density function γ_{l_I}, by replacing the Dirac-delta function $\delta_{\Gamma^I_{0i}}$ with γ_{l_I} as [60]:

$$\mathbf{F}^d = \mathbf{I} + \sum_{i=1}^{n} \mathbf{J}_i \otimes \mathbf{N}_i^I \gamma_{l_I} \tag{2.8}$$

2.1.3 Governing equations for coupled electromechanical and phase-field problem

The governing equations for the finite deformation coupled electromechanical and phase-field problem can be derived from the principle of virtual work [13]. In a Lagrangian formulation, the governing equations are expressed in the reference configuration are given as:

$$\underline{\text{Linear momentum}}: \quad \boldsymbol{\nabla}_{\mathbf{X}} \cdot \mathbf{P} + \mathbf{B} = 0 \quad \text{in}\,\Omega_0 \tag{2.9a}$$

$$\underline{\text{Gauss' law}}: \quad \boldsymbol{\nabla}_{\mathbf{X}} \cdot \mathbf{D} = Q_e \quad \text{in}\,\Omega_0 \tag{2.9b}$$

$$\underline{\text{Phase-field}}: \quad \boldsymbol{\nabla}_{\mathbf{X}} \cdot \boldsymbol{\xi}_0 - \pi_0 + \zeta_0 = 0 \,\text{in}\,\Omega_0 \tag{2.9c}$$

where $\mathbf{P}$ is the first P-K stress, $\mathbf{B}$ is the body force, $\mathbf{D}$ is the electric field displacement and Q_e is the applied charge density. $\boldsymbol{\xi}_0$ and π_0 are the internal microforces and power-conjugate corresponding to the phase-field order parameter. These quantities are given as:

$$\underline{\text{Mechanical}}: \quad \mathbf{P} = \rho_0 \frac{\partial \psi}{\partial \mathbf{F}} \tag{2.10a}$$

$$\underline{\text{Electrical}}: \quad \mathbf{D} = \rho_0 \frac{\partial \psi}{\partial \boldsymbol{\nabla}_{\mathbf{X}} \phi} \tag{2.10b}$$

$$\underline{\text{Phase-field}}: \quad \boldsymbol{\xi}_0 = \rho_0 \frac{\partial \psi}{\partial \boldsymbol{\nabla}_{\mathbf{X}} s} \text{ and } \pi_0 = \rho_0 \frac{\partial \psi}{\partial s} \tag{2.10c}$$

where $\rho_0 \psi$ is the Gibbs free energy density function detailed in the subsequent sections. The governing equations in Equation (2.9) is solved in a incremental fashion using the backward Euler method. A multi-pass staggered solution algorithm is adopted to solve for the coupled electromechanical phase-field problem [13].

2.2 Gibbs free energy density for degrading piezoelectric materials with interfaces

The constitutive equations for multiphase piezoelectric materials undergoing finite deformation electromechanical fracture are defined in terms of a Gibbs free energy density (GFED) function

under isothermal conditions. The GFED function proposed in this work is assumed to be the sum of the degraded stored energies and the fracture energy, and is expressed as:

$$\rho_0\psi = \rho_0\psi^M - \rho_0\psi^P - \rho_0\psi^E + \rho_0\psi^C \tag{2.11}$$

where $\rho_0\psi^M$ is the stored elastic energy density, $\rho_0\psi^P$ is the stored piezoelectric energy density, $\rho_0\psi^E$ is the electric energy densityand $\rho_0\psi^C$ is the crack surface energy density.

In case of piezocomposites wherein piezoelectric inclusions are embedded in an epoxy matrix. The GFED function for the inclusions which are active in nature is same as in Equation (2.11), whereas for the epoxy matrix that is passive (dielectric material with no electromechanical coupling) in nature, the GFED function is given as:

$$\rho_0\psi = \rho_0\psi^M - \rho_0\psi^E + \rho_0\psi^C \tag{2.12}$$

The energy terms in the GFED function are detailed in the following subsections.

2.2.1 Stored elastic energy density

When a material is degraded, its capacity to store elastic energy is reduced. To incorporate the effect of crack phase field on the load bearing capacity or strain energy of the material, the stored elastic energy density is formulated as:

$$\rho_0\psi^M = (1-s)^2\,\rho_0\psi^M_+ + \rho_0\psi^M_- \tag{2.13}$$

where $\rho_0\psi^M_+$ corresponds to the tensile and $\rho_0\psi^M_-$ corresponds to the compressive part of the strain energy. The split in Equation (2.13) allows for the tension-compression asymmetry or unilateral contact condition for fracture problems which assumes that only $\rho_0\psi^M_+$ i.e. the tensile part of the strain energy contributes to the degradation of the material. Many approaches have been proposed in the literature to account for tension-compression asymmetry in the phase-field models. However, most of these models are applicable to small deformation problems and materials with isotropic elasticity. These models are not sufficient for the piezoelectric inclusions that are generally transversely isotropic and undergo finite deformation. Recently, a new strain split has been proposed [19, 37] that accounts for both the unilateral contact condition as well as material anisotropy. It has been extended to a finite strain framework for crystal plasticity problems [28]. This formulation is adopted here for the stored elastic energy density of piezoelectric materials, expressed as:

$$\rho_0\psi^{M_{piezo}} = \frac{(1-s)^2}{2}\left\langle \widetilde{\mathbf{E}}^e_+, \widetilde{\mathbf{E}}^e_+ \right\rangle + \frac{1}{2}\left\langle \widetilde{\mathbf{E}}^e_-, \widetilde{\mathbf{E}}^e_- \right\rangle \tag{2.14}$$

where $\widetilde{\mathbf{E}}^e = \widetilde{\mathbf{E}}^e_+ + \widetilde{\mathbf{E}}^e_- = \sqrt{\mathbb{C}^e}$: $\mathbf{E}^e$ is the transformed Green-Lagrange strain tensor with $\mathbb{C}^e$ as the 4th order anisotropic elasticity tensor. $\langle \boxdot, \boxdot \rangle = \boxdot_{ij}\boxdot_{ij}$ denotes the standard inner product.

For the passive epoxy matrix, an isotropic Neo-Hookean type material model is assumed. The stored elastic energy for a degrading Neo-Hookean type material is given as [29, 59]:

$$\rho_0 \psi^{M_m} = (1-s)^2 \rho_0 \psi_+^{M_m} + \rho_0 \psi_-^{M_m} \tag{2.15}$$

where,

$$\rho_0 \psi_\pm^{M_m} = \frac{\mu}{2} \sum_{i=1}^{3} \left(\lambda_{i_\pm}^2 - 1 - 2\ln\lambda_{i_\pm} \right) + \frac{\kappa}{2} (\ln J_\pm)^2 \tag{2.16}$$

and,

$$\lambda_{i_+} = \begin{cases} \lambda_i & \text{for } \lambda_i > 1 \\ 1 & \text{otherwise} \end{cases} ; J_+ = \begin{cases} J & \text{for } J > 1 \\ 1 & \text{otherwise} \end{cases} \tag{2.17}$$

$$\lambda_{i_-} = \begin{cases} \lambda_i & \text{for } \lambda_i < 1 \\ 1 & \text{otherwise} \end{cases} ; J_- = \begin{cases} J & \text{for } J < 1 \\ 1 & \text{otherwise} \end{cases} \tag{2.18}$$

where μ is the shear modulus and κ is the bulk modulus of the material. λ_i are the stretches and J is the determinant of the deformation gradient. $\lambda_{i_\pm}$ and $J_\pm$ are the positive and negative components of the stretches and deformation gradient determinant respectively.

2.2.2 Stored piezoelectric energy density

Using arguments analogous to those for the stored elastic energy density, the stored piezoelectric energy density for a piezoelectric material is also split into a tensile and compressive part, as:

$$\rho_0 \psi^P = \mathscr{E} \cdot \mathbb{P} : \mathbf{E}_+^e + \mathscr{E} \cdot \mathbb{P} : \mathbf{E}_-^e \tag{2.19}$$

where $\mathscr{E}$ is the electric field and $\mathbb{P}$ is the 3rd order piezoelectric tensor. $\mathbf{E}_+^e$ and $\mathbf{E}_-^e$ corresponds to the tensile and compressive strain tensors respectively, obtained from the spectral decomposition of the Green-Lagrange strain tensor $\mathbf{E}^e$. Experimental results in the literature suggest that fracture processes in piezoelectric materials is driven by the mechanical part of the total electromechanical driving force. To successfully emulate the experimental observations, it has been shown that only half of the tensile stored piezoelectric energy density needs to be degraded [35, 55, 66]. Correspondingly, the stored piezoelectric energy in a degrading piezoelectric material is expressed as:

$$\rho_0 \psi^P = \frac{(1-s)^2}{2} \mathscr{E} \cdot \mathbb{P} : \mathbf{E}_+^e + \frac{1}{2} \mathscr{E} \cdot \mathbb{P} : \mathbf{E}_+^e + \mathscr{E} \cdot \mathbb{P} : \mathbf{E}_-^e \tag{2.20}$$

2.2.3 Stored electric energy density

The stored electric energy density for a piezoelectric or dielectric material is given as [13]:

$$\rho_0 \psi^E = \frac{J}{2} \left(\mathbf{F}^{-T} \mathscr{E}\right) \cdot \boldsymbol{\varepsilon} \left(\mathbf{F}^{-T} \mathscr{E}\right) \tag{2.21}$$

where J is the determinant of the total deformation gradient $\mathbf{F}$, $\boldsymbol{\varepsilon}$ is the 2nd order permittivity tensor and $\boxdot^{-T}$ denotes the inverse transpose of the tensor.

As discussed widely in literature [2, 35, 55, 65], there are three types of electrical boundary conditions that may be considered for the representation of crack face effects in piezoelectric materials. These are the permeable condition, impermeable condition and the energetically-consistent (EC) condition. While the permeable condition assumes that the electrical fields are not perturbed by the cracks, the impermeable and EC conditions acknowledge the existence of the cracks. However, unlike EC condition the impermeable condition neglects the effect of the medium filling the crack gaps. This might lead to some physical inconsistencies [2, 30]. To incorporate these crack face conditions, Equation (2.21) is modified as [13]:

$$\rho_0 \psi^E = \frac{J}{2} \left(\mathbf{F}^{-T} \mathscr{E}\right) \cdot \boldsymbol{\varepsilon}^{mod} \left(\mathbf{F}^{-T} \mathscr{E}\right) \tag{2.22}$$

where,

$$\underline{\text{Permeable}}: \quad \boldsymbol{\varepsilon}^{mod} = \boldsymbol{\varepsilon} \tag{2.23a}$$

$$\underline{\text{Impermeable}}: \quad \boldsymbol{\varepsilon}^{mod} = (1-s)^2 \boldsymbol{\varepsilon} \tag{2.23b}$$

$$\underline{\text{EC}}: \quad \boldsymbol{\varepsilon}^{mod} = (1-s)^2 \boldsymbol{\varepsilon} + (1-\eta)^2 \left\{1-(1-s)^2\right\} \varepsilon_m \mathbf{I} \tag{2.23c}$$

with ε_m denoting the permittivity of the medium filling the crack gaps.

2.2.4 Crack surface energy density

In phase-field models for homogeneous piezoelectric materials, the crack surface energy density is commonly formulated in terms of a Griffith type fracture energy per unit area, $\mathscr{G}_c$ and the regularized crack surface density function γ_{l_c} in Equation (2.3) as [35, 60]:

$$\rho_0 \psi^C = \frac{\mathscr{G}_c}{2 l_c} \left(s^2 + l_c^2 \nabla_{\mathbf{X}} s \cdot \nabla_{\mathbf{X}} s\right) \tag{2.24}$$

However, for multiphase piezoelectric composites, decohesion creates new surfaces at the interface leading to discontinuities in the displacement and electric potential fields. The energy required for

decohesion at the interface also needs to be accounted for. To incorporate this additional energy, the crack surface energy density is modified and expressed as [13]:

$$\rho_0 \psi^I = (1-\eta)^2 \mathscr{G}_c \gamma_{l_c} + \sum_{i=1}^{n} \rho_0 \psi_i^{int}(\mathbf{J}_i, \gamma_{l_I}, [\![\phi]\!]_i) \tag{2.25}$$

where $\rho_0 \psi_i^{int}(\mathbf{J}_i, \gamma_{l_I}, [\![\phi]\!]_i)$ is the energy density that accounts for the added mechanical and electrical energy contributions due to decohesion at the ith internal interface and is given as [13]:

$$\rho_0 \psi_i^{int} = \underbrace{\Phi(\Delta_{Ni}, \Delta_{Ti})\gamma_{l_I}}_{\text{mechanical}} - \underbrace{\frac{1}{2}\varepsilon_m \frac{[\![\phi]\!]_i^2}{\Delta_{Ni}}}_{\text{electrical}} \tag{2.26}$$

Here, $\Phi(\Delta_{Ni}, \Delta_{Ti})$ corresponds to the mechanical counterpart of the interface surface energy. It is represented by a cohesive zone potential function, which depends on the normal and tangential components of the displacement jump $\mathbf{J}_i$ denoted by Δ_{Ni} and Δ_{Ti} respectively [42]. The second term in Equation (2.26) corresponds to the electrical counterpart of the interface surface energy. This energy is the consequence of dielectric medium filling the crack gap creating local capacitor effect at the debonded interface [6]. However, it should be noted that this electrical energy contribution is only valid for the EC crack face electrical boundary conditions, that acknowledges the presence of the dielectric medium filled crack gaps.

2.3 Crack evolution and irreversibility criteria

The crack irreversibility condition is enforced through a history functional $\mathscr{H}$ [34, 35], which is defined as the maximum crack-driving energy ever experienced by an element during the deformation history. As suggested in literature [13, 35, 55, 66], the cracks are assumed to be driven only by the mechanical deformation. As such, only the tensile parts of the stored elastic and piezoelectric energy density is assumed to contribute to the crack-driving energy. The history functional and crack driving force are expressed as:

$$\mathscr{H} = \max_{[t,t+\Delta t]} [\mathfrak{H}_m, 0] \quad \text{with} \tag{2.27a}$$

$$\mathfrak{H}_m = \left\langle \widetilde{\mathbf{E}}_+^e, \widetilde{\mathbf{E}}_+^e \right\rangle - \mathscr{E} \cdot \mathbb{P} : \mathbf{E}_+^e \quad \text{(for piezoelectric material)} \tag{2.27b}$$

$$\mathfrak{H}_m = \frac{\mu}{2} \sum_{i=1}^{3} \left(\lambda_{i_+}^2 - 1 - 2\ln\lambda_{i_+}\right) + \frac{\kappa}{2}(\ln J_+)^2 \quad \text{(for epoxy matrix)} \tag{2.27c}$$

2.4 Numerical Examples

To demonstrate the capabilities of the coupled electromechanical and phase-field model, a set of representative 3D numerical simulations for multiphase piezoelectric composite materials subjected

Parameter	Value	Unit
ϕ_n	100	N/m
ϕ_t	100	N/m
σ_{max}	10	MPa
τ_{max}	10	MPa
λ_n	0.1	-
λ_t	0.1	-
α	3	-
β	3	-

Table 2.1: PPR model parameters and values. For details about the parameters refer [42]

to electromechanical loading conditions are performed. In the first example, a piezoelectric material with a weak interface is simulated to investigate the effect of the direction of external electric field on crack propagation along the interface. Next, a problem of bi-material system consisting of a pre-crack impinging on an interface is examined and the predictions from the model is compared against theoretical predictions. Finally, an example of heterogeneous piezocomposite microstructures with multiple piezoelectric fibers embedded in an epoxy matrix is simulated. This problem manifests a complex crack pattern evolution leading to complete failure of the piezocomposites. The influence of the fiber distribution on the global electromechanical response and effects of different electrical crack face conditions are also analyzed.

The 3D finite element models for the aforementioned examples uses a mesh of conventional 4-noded constant strain tetrahedral elements. Based on the parametric studies conducted in literature [38], l_I is taken to be the same as l_c. Also, the displacement and potential field jump regularization parameter h is taken to be half of l_c [38]. A mesh sensitivity analysis study is conducted to determine the mesh size that would sufficiently resolve the regularization length scale parameters l_c, l_I and h. The cohesive zone potential function used in this paper is based on the unified potential-based PPR model [42]. The model parameters of the PPR model and their values are listed in Table 2.1. These values have been used for characterizing the cohesive zone potential at the interfaces for all the examples in this work.

2.4.1 Piezoelectric material with weak interface

A piezoelectric material with a weak interface is considered in this example as shown in Figure 2.3. The dimensions of the specimen is taken as $1\text{mm}\times1\text{mm}\times0.02\text{mm}$. It has an initial pre-crack of length 0.5mm that is impinging on the interface. The model is mechanically loaded by an equal and opposite uniform displacement $u(t) = 2\text{e}^{-5}t$ respectively on the top and bottom XZ faces. A positive external electric field is applied along the X direction by applying steady state electric potentials of +500V and -500V on the left and right YZ faces respectively. The piezoelectric material is poled in the X direction and impermeable electrical crack face condition is considered. Material properties of the piezoelectric material are those of PZT-5H [44, 45], and are listed in Table 2.2. The fracture energy per unit area for the material is $\mathscr{G}_c = 150\text{N/m}$. The length scale parameters for this problem are chosen as $l_c = l_I = 2h = 0.01\text{mm}$.

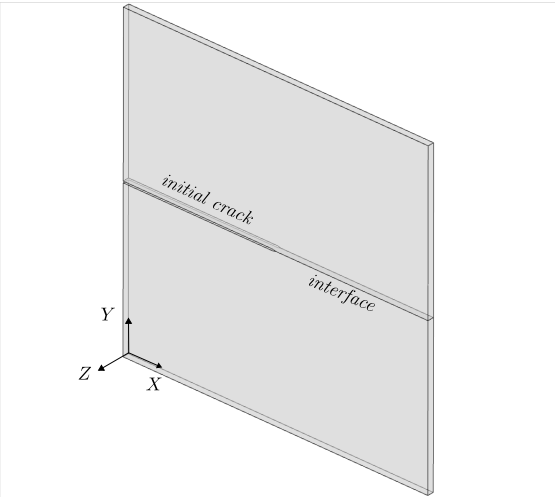

Figure 2.3: Schematic of specimen with an initial crack impinging on a cohesive interface.

Elastic Constants (GPa)				
C_{11}	C_{12}	C_{13}	C_{33}	C_{44}
126	55	53	117	35.5
Piezoelectric Constants $\left(C/m^2\right)$			**Dielectric Constants** (nF/m)	
P_{31}	P_{33}	P_{15}	ε_{11}	ε_{33}
-6.5	23.3	17	15.1	13.0

Table 2.2: Material parameters for PZT-5H [45]

Mesh sensitivity analysis: For the problem described above, the crack is expected to propagate along or near the interface. Therefore, the mesh is made finer in the domain where the crack is expected to propagate. Four finite element meshes of effective element sizes of $h_{eff} = \{2l_c = 0.02$mm, $l_c = 0.01$mm, $l_c/2 = 0.005$mm, $l_c/4 = 0.0025$mm$\}$ in the fine region are considered for the model. The meshes and the corresponding crack path evolution for the four meshes are illustrated in Figure 2.4. Though the simulations have been conducted in 3D, the meshes and crack profiles are shown in the XY plane for better visualization.

As can be see from Figure 2.4, the meshes with $h_{eff} = 2l_c$ and $h_{eff} = l_c$ predicts erroneous crack paths as the crack initiates from the bulk of the material instead of the crack tip. It is also observed that the cracks are very diffused as the mesh is unable to resolve the high gradient of the phase field order parameter s. However, for the meshes with $h_{eff} = l_c/2$ and $h_{eff} = l_c/4$, a much sharper crack is observed with the crack initiating at the crack tip and propagating along the interface. Though the mesh with $h_{eff} = l_c/4$ gives a sharper crack profile as compared to $h_{eff} = l_c/2$, the number of elements is significantly higher which is computationally expensive. From this, it can be concluded that the mesh with effective element size $l_c/2$ is sufficient to resolve the high gradient of s and

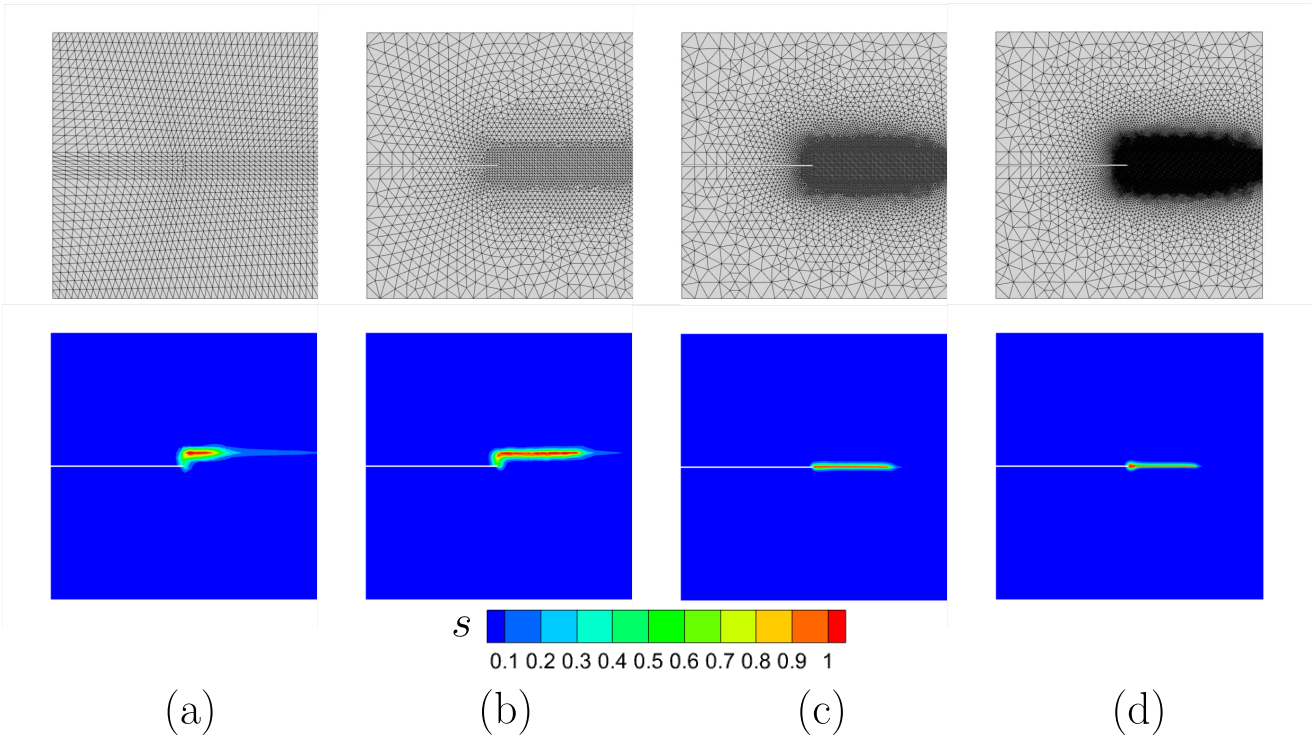

Figure 2.4: Finite element meshes and crack evolution profiles for effective element size (a) $2l_c$ =0.02mm (11648 elements) (b) l_c =0.01mm (25365 elements) (c) $l_c/2$ =0.005mm (149843 elements) (d) $l_c/4$ =0.0025mm (926791 elements)

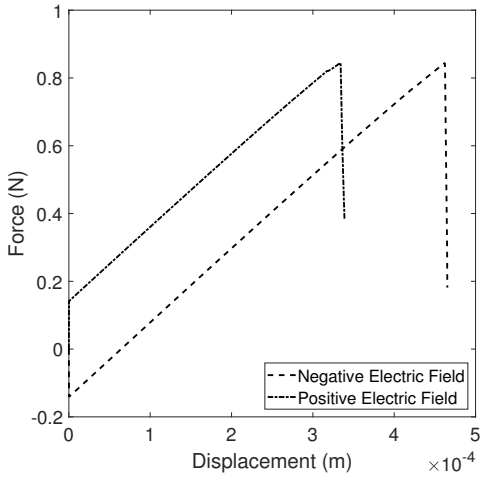

Figure 2.5: Load-displacement plot for piezoelectric material with weak interface.

predict correct crack path. For the subsequent simulations, the finite element mesh is chosen such that the effective element size is half the regularization length l_c.

Effect of external electric field: To investigate the effect of external electric field on crack evolution, two simulations are performed by applying positive and negative external electric fields along the X direction. The reaction force-displacement plots at the bottom XZ face for both the simulations are compared in Figure 2.5. From the plots it is observed that the drop in the reaction force for the negative electric field happens at a higher displacement value than the positive electric field. Therefore, it can be inferred that negative electric field delays the onset of the crack propagation while positive electric field promotes it. This observation is consistent with the theoretical trends reported in literature [17, 34].

2.4.2 Crack impinging on a piezoelectric bi-material interface

This example investigates the competition between penetration across the interface and deflection into the interface for a crack impinging on an interface of a piezoelectric bi-material. This problem has been analytically investigated using singular integral equations and maximum energy release rate criterion. According to the theoretical analysis, the criteria for a crack penetrating across the interface of a piezoelectric bi-material is given by[43–45]:

$$\frac{\mathscr{G}_p}{\mathscr{G}_d} > \frac{\mathscr{G}_c^1}{\mathscr{G}_c^{int}} \tag{2.28}$$

where $\mathscr{G}_c^1$ and $\mathscr{G}_c^{int}$ are the fracture toughness of material 1 and the interface respectively. $\mathscr{G}_p$ and $\mathscr{G}_d$ are the energy release rates for penetrating across the interface and deflecting into the interface.

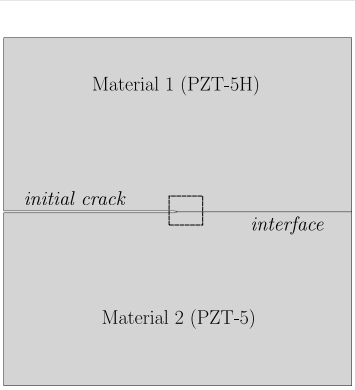

Figure 2.6: Schematic of piezoelectric bi-material specimen with an initial crack impinging on a cohesive interface separating material 1 and material 2.

Elastic Constants (GPa)				
C_{11}	C_{12}	C_{13}	C_{33}	C_{44}
121	75.4	75.2	111	22.8
Piezoelectric Constants $\left(C/m^2\right)$			**Dielectric Constants** (nF/m)	
P_{31}	P_{33}	P_{15}	ε_{11}	ε_{33}
-5.4	15.8	12.3	8.17	7.35

Table 2.3: Material parameters for PZT-5 [45]

The computational domain for the piezoelectric bi-material specimen is the same as shown in Figure 2.3. It consists of two materials with PZT-5H as material 1 and PZT-5 as material 2 [44, 45]. Figure 2.6 shows a 2D image of the XY plane for better visualization of the interface separating the materials. The model is mechanically loaded by an equal and opposite uniform displacement of $u(t) = 2\text{e}^{-5}t$ respectively on the top and bottom XZ faces. For this problem, the model is electrically loaded in the Y direction by applying a positive external electric field with steady state electric potentials of +500V and -500V on the top and bottom XZ faces respectively. Both materials 1 and 2 are poled in the X direction and impermeable electrical crack face condition is considered. The material properties of material 1 and 2 are listed in Table 2.2 and 2.3 respectively. The fracture energy per unit area for material 2 is taken as $\mathscr{G}_c^2 = 500\text{N/m}$, while $\mathscr{G}_c^1$ is varying.

From Equation (2.28), it is expected that for the bi-material specimen shown in Figure 2.6 an increase in the ratio $\mathscr{G}_c^1/\mathscr{G}_c^{int}$ will cause the crack evolution to transition from propagating into material 1 to propagating along the interface. Four simulations are carried out by varying the fracture energy per unit area for material 1, such that $\mathscr{G}_c^1/\mathscr{G}_c^{int} = \{0.2, 0.6, 1.0, 1.5\}$. Since this problem is concerning the path that a crack follows when it is at the interface of the piezoelectric bi-material, attention is focused on the domain bounded by dotted lines in Figure 2.6. The crack profiles are shown in Figure 2.7. As can be seen, for $\mathscr{G}_c^1/\mathscr{G}_c^{int} = 0.2$ and 0.6, the crack penetrates into material 1. For $\mathscr{G}_c^1/\mathscr{G}_c^{int} = 1.0$ the crack initially propagates along the interface and then penetrates into

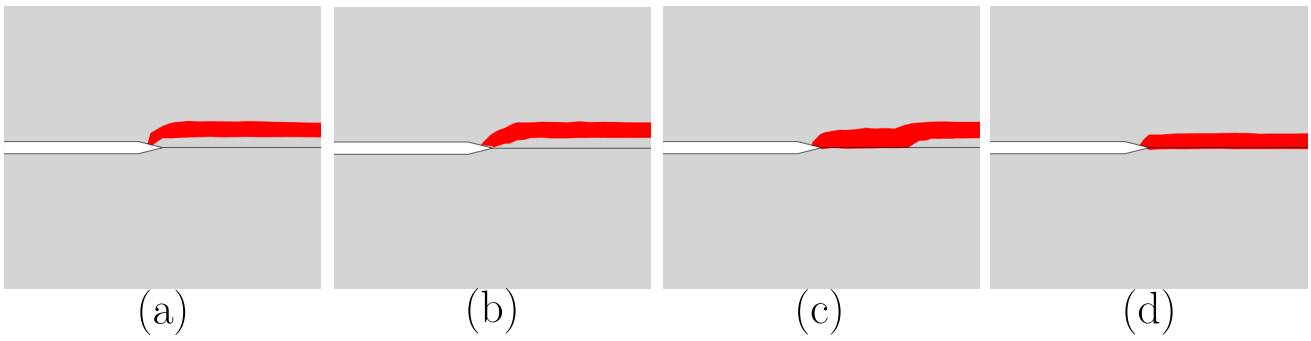

Figure 2.7: Crack evolution profile in piezoelectric bi-material specimen for (a) $\mathscr{G}_c^1/\mathscr{G}_c^{int} = 0.2$ (b) $\mathscr{G}_c^1/\mathscr{G}_c^{int} = 0.6$ (c) $\mathscr{G}_c^1/\mathscr{G}_c^{int} = 1.0$ (d) $\mathscr{G}_c^1/\mathscr{G}_c^{int} = 1.5$. The phase field order parameter $s \geq 0.9$ is visualized.

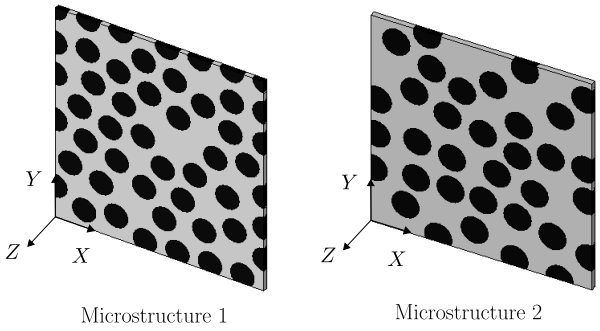

Figure 2.8: Schematic of piezocompostie microstructures with different fiber distributions

material 1. Finally, for $\mathscr{G}_c^1/\mathscr{G}_c^{int} = 1.5$, the crack propagates entirely along the interface indicating decohesion at the interface. This example elucidates that the proposed model is able to capture the trend predicted from theoretical analyses.

2.4.3 Piezocomposite microstructure with randomly distributed fibers

Two nonuniform piezocomposite microstructures consisting of randomly distributed piezoelectric fibers of radius 0.125mm embedded in a relatively compliant matrix is considered in this example. The piezocomposite specimens have a domain size of 2mm $\times$ 2mm $\times$ 0.05mm as shown in Figure 2.8. The fiber distribution is generated using a code developed by the Composites Design and Manufacturing Hub [4, 5]. The domain is mechanically loaded in uniaxial tension by restraining the bottom XZ face and applying a prescribed displacement of $u(t) = 2e^{-5}t$ mm on the top XZ face. Additional boundary conditions are applied to restrict any rigid body motion. An external electric field is applied in the Y direction via steady state electric potentials of -125V and +125V on the bottom and top XZ faces respectively. The piezoelectric fibers considered in this example are PZT-5A1 [20] with material properties listed in Table 2.4 and are poled in the Y direction. The passive matrix is isotropic and dielectric in nature with material properties: $\mu = 1GPa, \kappa = 2.17GPa$ and $\varepsilon = 0.04nF/m$. The length scale parameters for this problem are chosen as $l_c = l_I = 2h = 0.02$mm. Since the crack paths are not known *a-priori*, entire domain is uniformly meshed with effective element size of 0.01mm.

Elastic Constants (GPa)				
C_{11}	C_{12}	C_{13}	C_{33}	C_{44}
129.3	91.6	87.1	116.8	9.7
Piezoelectric Constants $\left(C/m^2\right)$			**Dielectric Constants** (nF/m)	
P_{31}	P_{33}	P_{15}	ε_{11}	ε_{33}
-2.7	19.2	5.5	17.3	16.4

Table 2.4: Material parameters used for the active piezoelectric fibers (PZT-5A1) [20]

Three simulations are performed considering the three types of electrical crack face conditions, viz. permeable, impermeable and energetically consistent (EC) conditions. For the EC condition the dielectric permittivity of the medium filling the crack gaps is taken as $\varepsilon_m = 22.56e^{-3}nF/m$. Crack evolution profiles in both the microstructures with EC crack face condition are shown in Figure 2.9. As observed, failure initiates with simultaneous debonding at different fiber-matrix interfaces followed by the propagation of the crack into the epoxy matrix. With increasing load, an intricate array of crack pattern evolves resulting from a series of successive debonding and matrix cracking. Finally, it is seen that the cracks coalesce into a dominant crack path that leads to complete degradation of the microstructure. The plots corresponding to the reaction force and electrical charge accumulated against displacement at the bottom XZ face are illustrated in Figure 2.10 and 2.11 respectively. The plots also manifest the loss in load carrying capacity of the speciemens. This problem demonstrates that the coupled electromechanical and phase-field model is able to illustrate the transition of cracks from interfacial decohesion to matrix cracking, as well as the complex interactions among multiple cracks. Similar crack evolution profiles are observed for the permeable and impermeable conditions.

Effect of fiber distribution on the electromechanical response of piezocomposites: From the plots in Figure 2.10 and 2.11, it is observed that the peak force and accumulated electric charge are different. This difference in the electromechanical response may be attributed to local clustering of fibers that influence the initiation and propagation of the cracks. The influence of the distribution of the fibers becomes very important while calibrating parametrically upscaled models [71, 72] that has explicit microstructural dependencies on the macroscopic response of structural scale analysis.

Evolution of electric field for different electrical crack face conditions: The electric field evolution in the piezocomposites is illustrated next. Contour plots of the Y component of electric field in the cracked speciemen of both the microstructures are plotted in Figure 2.12. The XY plane is shown for better visualization. As can be seen in the plots, for permeable condition the electric field distribution is not affected by the presence of cracks in the domain. This observation can be associated with the assumption of permeable condition that the electric fields in the degraded material is not affected by the evolution of crack. In case of impermeable condition, very high electric field is concentrated in the crack gaps. This is because as soon as a crack is formed, the permittivity of the material $\varepsilon \to 0$ which leads to a very high electric field across the crack gap.

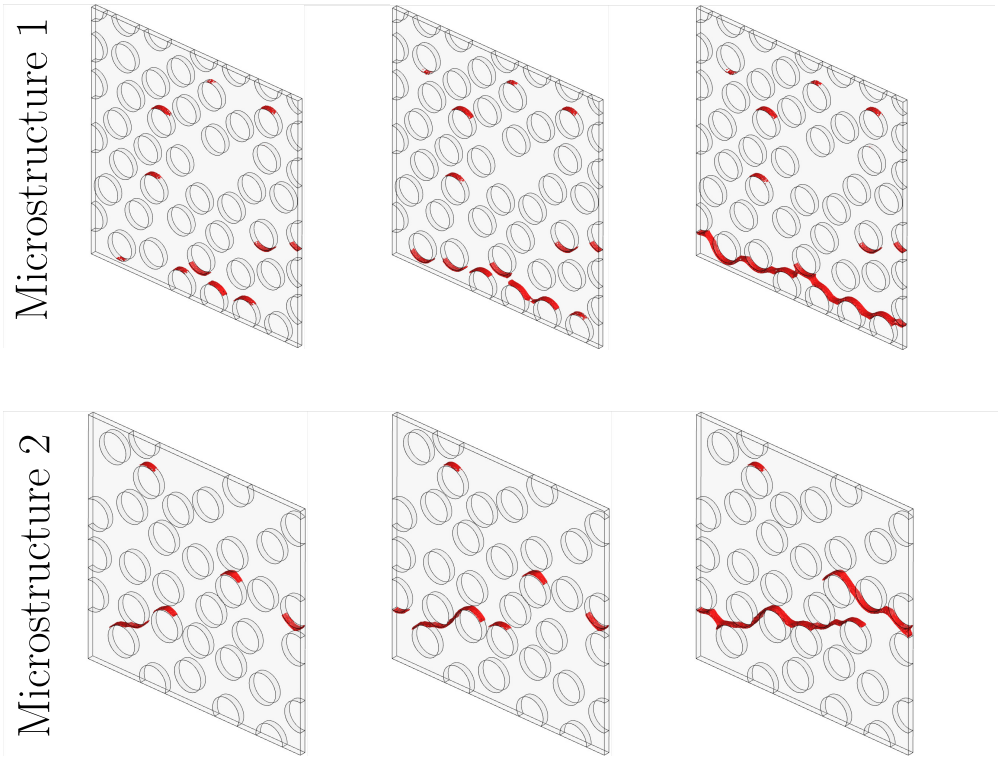

Figure 2.9: Crack evolution profile in piezocomposite microstructures at different time steps . The phase field order parameter $s \geq 0.95$ is visualized. $\eta = 1$ delineates the interfaces in the computational domain.

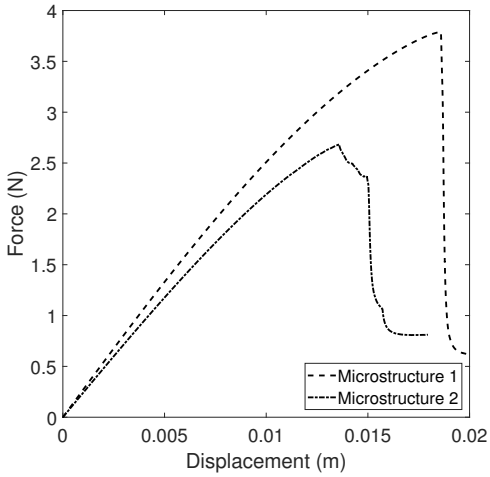

Figure 2.10: Load-displacement plot for piezocomposite microstructures.

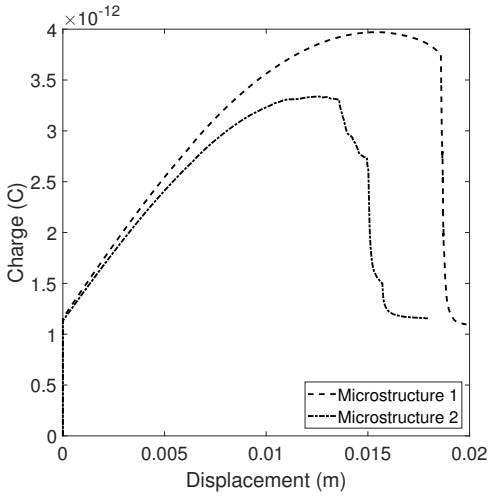

Figure 2.11: Charge-displacement plot for piezocomposite microstructures.

The EC crack face condition also exhibits a high concentration of electric field within the crack. However, in comparison to permeable condition a smoother transition of the electric field is observed around the crack for EC condition. This is owing to the dielectric effect of the medium filling the crack gap, that allows for a smoother distribution of electric field. This is consistent with the observations made for fracture in homogeneous piezoelectric material [55].

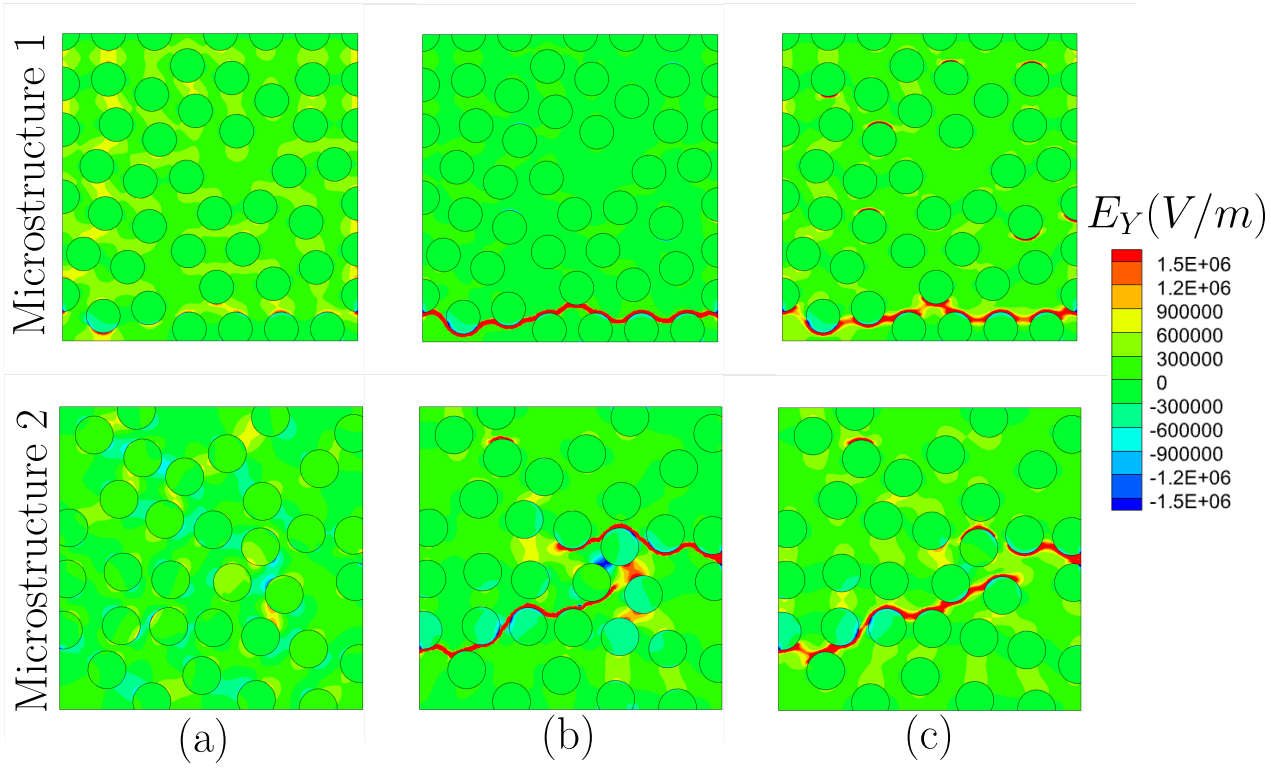

Figure 2.12: Electric field in the cracked speciemens of the piezocomposite microstructures for (a) permeable (b) impermeable (c) energetically consistent electrical crack face conditions.

Chapter 3

Developing a Virtual Damage Sensor Using A Coupled Electro-Mechanical FE Model of a Piezoelectric Material

Piezoelectric materials are in increasing demand in a variety of applications including actuators, sensors, robotics, energy harvesters, structural health monitoring, stretchable electronics etc. [10, 12, 25, 47, 70, 73]. These materials develop coupled mechanical and electrical fields when subjected to electrical or mechanical loading due to complex multi-physics interactions. Piezoelectric materials form intrinsic sensors of mechanical states since they convert mechanical energy into the electric energy and vice versa. Smart structures of piezoelectric materials undergoing finite deformation are used in vibration control and energy harvesting, e.g. in [15, 21]. A number of piezoelectric structural applications consist of advanced composite materials, where the piezoelectric material is bonded to an elastic substrate or embedded in a laminated composite structure [10, 12, 25]. Under conditions of finite deformation, these composite structures can undergo damage and delamination, thus reducing their performance capability. Damage in composite smart structures initiate at the microstructural scale as interfacial debonding and propagate by crack growth, thus affecting the piezoelectric material properties. Structural health monitoring (SHM) is needed within their life-cycle for predicting reliability through detection of damage and potential failure sites. Commonly used SHM methods incorporate strain gauges, optical fibers, eddy current, acoustic emission, or lamb wave analysis, often for qualitative prediction of damage. Robust computational models coupling mechanical and electrical fields in the presence of damage are needed for effective design of piezoelectric systems.

A number of theoretical and computational models have been proposed for coupling mechanical, electrical and magnetic fields for substrates undergoing finite deformation, viz. [11, 24, 26, 31, 33, 41, 57, 61–63]. In [70] finite deformation in piezoelectric materials is modeled with constitutive equations written in the current configuration. A finite deformation variational formulation for piezoelectric materials has been conducted in [36], where the strain and electric displacements are derived from deformation and electric vector potential-dependent free energy. Cracks and interfaces in piezo-electric ceramic materials have been studied in [56] by simultaneously solving a

macroscopic crack tip problem along with microscopic irreversible processes near the crack tip. The change in piezoelectric material properties under high electrical and mechanical stresses have been studied in [9], while damage of piezoelectric ceramics under cyclic loading has been studied in [40]. While the piezoelectric constant d_{33} has been found to decrease with increasing cycles at a critical applied stress, the electromechanical coupling coefficient is not significantly affected by cyclic loading. A piezoelectric damage model is introduced in [69] that reveals that the piezoelectric material property is affected by both mechanical and electric damage. Ghosh and his group has developed a generalized framework to couple dynamical mechanical and transient electromagnetic fields in a total Lagrangian formulation in [18, 68]. A wavelet transformation induced multi-time scaling (WATMUS) algorithm has been developed to account for disparate time-scales in multi-physics coupling for mechanical-electromagnetic problems in [68] and mechanical-piezoelectric problems [67].

In this work, a finite element formulation is developed for finite deformation of piezoelectric materials undergoing mechanical damage. A total Lagrangian formulation is invoked for analyzing the influence of the evolving mechanical fields undergoing damage on the electrical fields in the coupled platform. A phenomenological continuum damage mechanics model is used to represent the material behavior. A staggered coupling is invoked between the mechanical and electric fields following the framework developed in [18]. The electric fields undergo changes with damage and a model is established to correlate the electric field evolution with damage.

The chapter begins with a discussion on the governing equations for the coupled electric and dynamical field under finite deformation conditions in section 3.1. Finite deformation equations with evolving damage is discussed in section 3.1.1, while piezoelectric equations are established in section 3.1.2. Section 3.2 develops the weak forms and finite element implementation of the coupled mechanical-piezoelectric problem. Numerical studies for validating the coupled dynamics and electric field model and code for the piezoelectric material are conducted in section 3.3. Section 3.4 develops a coupled piezoelectric damage sensor using the coupled piezoelectric model.

3.1 Governing Equations for the Coupled Electric and Dynamical Mechanical Field under Finite Deformation

Modeling coupled electrical and mechanical fields for piezoelectric materials requires concurrent solution of the governing equations of motion and electric balance laws with nonlinear piezoelectric constitutive relations. In this section the governing and constitutive equations for the finite deformation dynamical fields and electric fields in the Lagrangian description are discussed.

3.1.1 Finite Deformation Dynamics Equations with Evolving Damage in Reference Configuration

The mechanical response of the piezoelectric material is modeled using governing equations for a hyper-elastic material undergoing finite deformation under dynamic loading conditions. In the

total Lagrangian formulation, the reference configuration at a time t_0, $\Omega_0(=\Omega(t_0))$, is expressed in terms of the material coordinates $X_I,\ I=1,2,3$, while the current configuration at time t, $\Omega(t)$, is represented by the spatial coordinates $x_i,\ i=1,2,3$. The mapping between the deformed and undeformed reference configuration is expressed in terms of the deformation gradient and displacement fields as:

$$F_{iJ}=\frac{\partial x_i}{\partial X_J}=\delta_{iJ}+\frac{\partial u_i}{\partial X_J},\ \text{where}\ \ u_i(X_J,t)=x_i-\delta_{iJ}X_J \tag{3.1}$$

The Jacobian of the mapping $J=det(F_{iJ})>0$. The dynamic equilibrium equations in the current configuration is given as:

$$\frac{\partial\, {}^t\sigma_{ij}}{\partial\, {}^t x_j}+{}^t\rho b_i={}^t\rho\ddot{u}_i \tag{3.2}$$

where ${}^t\sigma_{ij}$ is the Cauchy stress, b_i is the body force per unit mass and ${}^t\rho$ is the density in the deformed configuration. The corresponding equilibrium equation in the reference configuration Ω_0 is derived as:

$$\frac{\partial\, {}^t_0P_{iJ}}{\partial X_J}+{}^0\rho b_i={}^0\rho\ddot{u}_i\quad\text{where}\quad {}^0\rho=J\,{}^t\rho,\quad\text{and}\quad {}^t_0P_{iJ}=J\,{}^t\sigma_{ij}F^{-1}_{Jj} \tag{3.3}$$

where ${}^t_0P_{iJ}$ is the first Piola-Kirchhoff stress and ${}^0\rho$ is the density in the reference configuration. The corresponding second Piola-Kirchhoff stress and its conjugate, the Green Lagrangian strain are defined as:

$$S_{IJ}=J\frac{\partial X_J}{\partial x_m}\frac{\partial X_I}{\partial x_n}\sigma_{mn}\quad\text{and}\quad E_{IJ}=\frac{1}{2}\left(C_{IJ}-\delta_{IJ}\right) \tag{3.4}$$

where $C_{IJ}=F_{kI}F_{kJ}$ is the right Cauchy-Green deformation tensor.

The finite deformation material response is defined by hyperelastic constitutive relations for a compressible Neo-Hookean material. Following ideas for the mechanical damage model proposed in [32, 53], the stored mechanical energy density $\Psi^{ME}(E_{IJ})$ of the hyperelastic material is decomposed into a volumetric (Ψ^{vol}) and deviatoric (Ψ^{dev}) energy density as:

$$\Psi^{ME}=\Psi^{vol}+\Psi^{dev} \tag{3.5}$$

where

$$\Psi^{vol}=\frac{1}{2}(\lambda+\frac{2}{3}\mu)\left[\frac{1}{2}\left(J^2-1\right)-lnJ\right] \tag{3.6a}$$

$$\Psi^{dev}=\frac{1}{2}\mu(\bar{I}_C-3) \tag{3.6b}$$

Here λ and μ are Lam*é* constants. $\bar{I}_C$ is the first invariant of $\overline{C}_{IJ}=\overline{F}_{kI}\overline{F}_{kJ}$, where $\overline{F}_{iJ}$ is a volume preserving deformation gradient defined as

$$\overline{F}_{kI}=J^{-\frac{2}{3}}F_{kI}\qquad\text{such that}\qquad \det(\overline{F}_{kI})=1 \tag{3.7}$$

The second Piola-Kirchoff stress S_{IJ}^{ME} may correspondingly be decomposed into volumetric and deviatoric parts as:

$$S_{IJ}^{vol} = 2\frac{\Psi^{vol}}{C_{IJ}} = \frac{1}{2}(\lambda + \frac{2}{3}\mu)\left(J^2 - 1\right)C_{IJ} \tag{3.8a}$$

$$S_{IJ}^{dev} = 2\frac{\Psi^{dev}}{C_{IJ}} = \mu J^{-2/3}\left[\delta_{IJ} - \frac{1}{3}C_{IJ}^{-1}I_C\right] \tag{3.8b}$$

Representing damage and its evolution

An isotropic damage model is considered in this work. The mechanical state dependent damage is represented by a scalar damage parameter $D \in [0,1)$, which results in a reduction of the elastic stiffness and piezoelectric properties of the material. Following [32, 53], the damage is confined to the deviatoric part of the strain energy. Consequently the mechanical free energy density is decomposed into volumetric and deviatoric terms as:

$$\Psi^{ME}\left(J, \overline{C}_{IJ}, D\right) = \Psi^{vol}\left(J\right) + (1-D)\,\Psi^{dev}\left(\overline{C}_{IJ}\right) \tag{3.9}$$

The mechanical state-dependent damage evolution law in [53] expresses the damage parameter in terms of an effective maximum equivalent strain as $D(\Xi^{max})$, where the equivalent strain is defined as:

$$\Xi^{max} = \underset{s\in(-\infty,t]}{max}\sqrt{2\Psi_0^{dev}\left(\overline{C}_{IJ}\right)} \tag{3.10}$$

Here Ψ_0^{dev} is the initial deviatoric strain energy density. A strain-space damage criterion is proposed for the deformation history as:

$$\hat{\varphi}\left(E_{IJ}, \Xi^{max}\right) = \Xi^{max} - \sqrt{2\Psi_0^{dev}\left(\overline{C}_{IJ}\right)} \geq 0 \tag{3.11}$$

The normal to the damage surface is defined as:

$$N_{IJ} = \frac{\partial\hat{\varphi}}{\partial E_{IJ}} = \frac{1}{\Xi^{max}}\frac{\partial\Psi_0^{dev}}{\partial E_{IJ}} \tag{3.12}$$

Damage increases irreversibly in this criterion, when loaded from a damage state. The evolution law is represented by a nonlinear function of the history-dependent maximum equivalent strain Ξ^{max} as:

$$\dot{D} = \begin{cases} \dot{D}(\Xi^{max}) & \text{if} \quad \hat{\varphi} = 0 \qquad \text{and} \quad \boldsymbol{N} : \boldsymbol{E} > 0 \\ 0 & \text{otherwise} \end{cases} \tag{3.13}$$

In [53], a saturation function has been used for the damage parameter $D(\Xi^{max})$ as:

$$D = 1 - g\left(\Xi^{max}\right) \ , \quad \text{where the function} \quad g\left(x\right) = \beta + (1-\beta)\frac{1-e^{-x/\alpha}}{x/\alpha} \tag{3.14}$$

Here $\alpha \in (0,\infty)$ is the saturation rate and $\beta \in [0,1]$ represents the damage limit. When the damage criterion (3.11) is met, evolution of D is given as:

$$\dot{D} = -\frac{g'(\Xi^{max})}{\Xi^{max}}\frac{\partial\Psi_0^{dev}}{\partial E_{IJ}}\dot{E}_{IJ} \quad \text{with} \quad g'(x) = \frac{1-\beta}{\alpha}\frac{e^{-x/\alpha} - \frac{1-e^{-x/\alpha}}{x/\alpha}}{x/\alpha} \leq 0 \tag{3.15}$$

This guarantees the condition $\dot{D} \geq 0$ for $\alpha \in (0,\infty)$ and $\beta \in [0,1]$.

3.1.2 Piezoelectric Equations in Reference Configuration

A Lagrangian description is invoked for piezo-electricity under the conditions of finite deformation. The Maxwell's equations for electro-magnetic fields have been derived in the reference configuration in [18, 24, 62, 63]. For piezoelectric applications, the magnetic field effects, free charge density and conducting current are neglected, thus reducing the Maxwell's equations to the following relations:

$$D_{I,I} = 0 \qquad \text{Gauss' law of electricity} \tag{3.16a}$$

$$\varepsilon_{IJK}\frac{\partial}{\partial X_J}E_K = 0 \qquad \text{Faraday's law} \tag{3.16b}$$

where D_I and E_I are the electric displacement and electric fields in the reference configuration respectively. These variables are related to their respective values in the current configuration through the Piola transformation as:

$$D_I = JX_{I,j}d_j, \quad E_I = e_j x_{j,I} \quad \text{and} \quad Q_e = Jq_e$$

The permutation operator ε_{IJK} in the reference configuration is expressed in terms of that in the current configuration ε_{ijk} as:

$$\varepsilon_{IJK} = J^{-1}\varepsilon_{ijk}x_{i,I}x_{j,J}x_{k,K} \tag{3.17}$$

For solving equations (3.16) a scalar potential φ has been proposed as primary variables for the electric field in [18, 24]. In the reference configuration, it is expressed as:

$$E_I = e_j x_{j,I} = -\varphi_{,j}x_{j,I} = -\Phi_{,I} \tag{3.18}$$

where φ and Φ are the electric potentials in the current and reference configurations respectively. The electric displacement field is related to the electric field through the constitutive relation:

$$D_I = \varepsilon JC_{IJ}^{-1}E_J + P_I \tag{3.19}$$

where ε is the permittivity, C_{IJ} is the right Cauchy-Green deformation tensor and P_I is the polarization of the electric field. For piezoelectric materials, P_I corresponds to a term induced by piezo-electricity. Substituting equations (3.18) and (3.19) into equation (3.16a) yields the governing equation in terms of the scalar potential as:

$$\left(\varepsilon JC_{IJ}^{-1}\Phi_{,J} - P_I\right)_{,I} = 0 \tag{3.20}$$

Piezoelectric material constitutive equations with damage model in reference configuration

A enthalpy density-based Hamilton's principle has been proposed for solving coupled mechanical and electrical problems of piezoelectric materials in [33, 39]. Following this concept, an explicit form for the enthalpy density in the reference configuration is proposed for a piezoelectric material, undergoing damage as:

$$\mathscr{H}(E_{IJ}, E_K, D) = \Psi^{ME}\left(J, \overline{C}_{IJ}, D\right) - \hat{\mathscr{P}}_{KIJ}(D)E_{IJ}E_K - \frac{1}{2}\varepsilon JC_{IJ}^{-1}E_I E_J \tag{3.21}$$

where $\Psi^{ME}\left(J,\overline{C}_{IJ},D\right)$ is the stored energy density for the hyperelastic material undergoing damage in equation (3.9). The second term is the energy density due to the coupled fields, where $\hat{\mathscr{P}}_{KIJ}(D)$ is a damage dependent piezoelectric coupling tensor and the third term is the energy density due to electric fields. For simplicity, a linear damage relation is assumed for the piezoelectric tensor, i.e.

$$\hat{\mathscr{P}}_{KIJ}(D) = (1-D)\hat{\mathscr{P}}^{0}_{KIJ}(D) \tag{3.22}$$

This reduces the enthalpy density to:

$$\mathscr{H} = \Psi^{vol}(J) + (1-D)\Psi^{dev}\left(\overline{C}_{IJ}\right) - (1-D)\hat{\mathscr{P}}^{0}_{KIJ}E_{IJ}E_K - \frac{1}{2}\varepsilon JC^{-1}_{IJ}E_IE_J \tag{3.23}$$

The second law of thermodynamics yields the Clausius-Planck free energy density inequality indicating that the internal dissipation is non-negative, i.e. $\mathscr{D}_{int} \geq 0$. Neglecting thermal effects, this inequality for the coupled piezoelectric system in the presence of damage may be written as:

$$\mathscr{D}_{int} = S_{IJ}\dot{E}_{IJ} - \dot{\mathscr{H}} - \dot{E}_I D_I \geqslant 0 \tag{3.24}$$

Since $\mathscr{H}$ is a function of D, J, $\overline{C}_{IJ}$ and E_K, the time derivative of the electric enthalpy is expressed as:

$$\dot{\mathscr{H}} = \frac{\partial \mathscr{H}}{\partial J}\dot{J} + \frac{\partial \mathscr{H}}{\partial \overline{C}_{IJ}}\dot{\overline{C}}_{IJ} + \frac{\partial \mathscr{H}}{\partial E_K}\dot{E}_K + \frac{\partial \mathscr{H}}{\partial D}\dot{D} \tag{3.25}$$

where the rates are derived as:

$$\dot{J} = \frac{\partial J}{\partial C_{IJ}}\dot{C}_{IJ} = \frac{J}{2}C^{-1}_{IJ}\dot{C}_{IJ} \tag{3.26a}$$

$$\dot{\overline{C}}_{IJ} = \frac{\partial \overline{C}_{IJ}}{\partial C_{IJ}}\dot{C}_{IJ} = \frac{\partial \overline{C}_{IJ}}{\partial C_{KL}} = \frac{\partial J^{-2/3}}{\partial C_{IJ}} = J^{-2/3}\left(\mathbb{I}_{IJKL} - \frac{1}{3}C_{IJ}\otimes C^{-1}_{KL}\right)\dot{C}_{IJ} \tag{3.26b}$$

The constitutive equations for the coupled piezoelectric system undergoing damage is derived from equations (3.24) and (3.25) as:

$$S_{IJ} = \frac{\partial \mathscr{H}}{\partial E_{IJ}} = 2\frac{\partial \Psi^{vol}}{\partial C_{IJ}} + 2(1-D)\frac{\partial \Psi^{dev}}{\partial C_{IJ}} - \frac{\partial}{\partial E_{IJ}}\left[(1-D)\hat{\mathscr{P}}_{KIJ}E_{IJ}E_K\right] - \frac{\partial}{\partial E_{IJ}}\left[\frac{1}{2}\varepsilon JC^{-1}_{IJ}E_IE_J\right] \tag{3.27a}$$

$$D_I = -\frac{\partial \mathscr{H}}{\partial E_I} = \varepsilon JC^{-1}_{JI}E_J + (1-D)\hat{\mathscr{P}}_{IJK}E_{JK} \tag{3.27b}$$

Combining equation (3.27b) with equation (3.19), the piezoelectricity induced polarization vector for the damaging material is deduced to be:

$$P_I = (1-D)\hat{\mathscr{P}}_{IJK}E_{JK} \tag{3.28}$$

Equation (3.27a) may be expanded using equations (3.5) and (3.8) as:

$$S_{IJ} = \underbrace{S^{vol}_{IJ} + (1-D)S^{dev}_{IJ}}_{S^{ME}_{IJ}} - \underbrace{(1-D)\hat{\mathscr{P}}_{KIJ}E_K}_{S^{Piezo}_{IJ}} - S^{Maxwell}_{IJ} \tag{3.29}$$

Here S_{IJ}^{vol} and S_{IJ}^{dev} have been defined in equations (3.8a) and (3.8b) respectively, and the Maxwell stress in the reference configuration is given as [36]:

$$S_{IJ}^{Maxwell} = \frac{1}{2}\varepsilon J\left[\left(E_P C_{PQ}^{-1} E_Q\right) C_{IJ}^{-1} - E_p E_Q\left(C_{PI}^{-1} C_{JQ}^{-1} + C_{PJ}^{-1} C_{IQ}^{-1}\right)\right] \tag{3.30}$$

It can be proved that the Maxwell stress in the reference configuration follows the Piola transformation from that defined in the current configuration [8, 11, 31]. The internal dissipation inequality of equation (3.24) is written as:

$$\mathscr{D}_{int} = \left(\Psi^{dev} - \hat{\mathscr{P}}_{KIJ} E_{IJ} E_K\right)\dot{D} \geqslant 0 \tag{3.31}$$

Thus the damage conjugate force $\left(\Psi^{dev} - \hat{\mathscr{P}}_{KIJ} E_{IJ} E_K\right)$ should be semi-positive definite to guarantee monotonic increase of the damage parameter.

3.2 Weak Forms and Finite Element Implementation

The mechanical problem for the finite deformation problem with path dependent damage is solved incrementally using an updated Lagrangian formulation. The electric field problem, on the other hand is one-way coupled and depends on the value of the instantaneous damage variable. Hence, it is solved using a total Lagrangian formulation at each step.

3.2.1 Mechanical Field for Deforming Piezoelectric Material with Damage

In the updated Lagrangian formulation, the incremental nonlinear weak form is set up between the reference deformed configuration at time t and the unknown deformed configuration at time $t+\Delta t$. The principle of virtual work is formulated corresponding to the strong form of equation (3.3) for the increment t to $t+\Delta t$ in the reference configuration at time t. Multiplying by the virtual displacement $\delta u_i = \delta U_I$ and integrating over the volume Ω_t in the reference configuration, the weak form is given as:

$$\int_{\Omega_t} \frac{\partial\, {}_t^{t+\Delta t}P_{iJ}}{\partial\, {}^tX_J}\delta u_i d\Omega_t + \int_{\Omega_t} {}^t\rho b_i \delta u_i d\Omega = \int_{\Omega_t} {}^t\rho \ddot{u}_i \delta u_i d\Omega \tag{3.32}$$

where ${}_t^{t+\Delta t}P_{iJ} (= {}_t^{t+\Delta t}J\, {}^{t+\Delta t}\sigma_{ik}\, {}_t^{t+\Delta t}F_{Jk}^{-1} = \frac{\partial\, {}^{t+\Delta t}x_i}{\partial\, {}^tX_K}\, {}_t^{t+\Delta t}S_{KJ})$ is the first Piola-Kirchhoff stress, ${}^t\rho$ is the density in the updated reference configuration and b_i is the body force per unit mass. Applying the divergence theorem and integrating by parts, the weak form reduces to:

$$\int_{\Omega_t} {}_t^{t+\Delta t}P_{iJ}\frac{\partial \delta u_i}{\partial\, {}^tX_J}d\Omega + \int_{\Omega_t} {}^t\rho \ddot{u}_i \delta u_i d\Omega = \int_{\Gamma_t} {}_t^{t+\Delta t}P_{iJ}\delta u_i\, {}^tN_J d\Gamma + \int_{\Omega_t} {}^t\rho b_i \delta u_i d\Omega \tag{3.33}$$

With the traction increment given as ${}_t^{t+\Delta t}T_I = {}_t^{t+\Delta t}P_{iJ}\, {}^tN_J = \bar{T}_I^t$ on Γ_t, the weak form is re-written as:

$$\int_{\Omega_t} {}_t^{t+\Delta t}P_{iJ}\frac{\partial \delta u_i}{\partial\, {}^tX_J}d\Omega = \int_{\Gamma_t} \bar{T}_I^t \delta u_i d\Gamma + \int_{\Omega_t} {}^t\rho b_i \delta u_i d\Omega - \int_{\Omega_t} {}^t\rho \ddot{u}_i \delta u_i d\Omega \tag{3.34}$$

Using the relations between first and second Piola-Kirchoff stresses and definitions of the Green-Lagrangian strain tensor in equation (3.34) leads to the equation:

$$\int_{\Omega_t} {}^{t+\Delta t}_{t}S_{MN}\delta\,{}^{t+\Delta t}_{t}E_{MN}d\Omega = \int_{\Gamma_t} \overline{T}^{t}_{I}\delta u_i d\Gamma + \int_{\Omega_t} {}^{t}\rho b_i \delta u_i d\Omega - \int_{\Omega_t} {}^{t}\rho \ddot{u}_i \delta u_i d\Omega \tag{3.35}$$

In the presence of damage, the deviatoric part of second P-K stress S^{dev}_{MN} and the piezoelectric coupling coefficient $\hat{\mathscr{P}}_{IMN}$ will be affected by damage. Incorporating the stress decomposition of equation (3.29) in equation (3.35), the weak form becomes:

$$\begin{aligned}
&\int_{\Omega_t} {}^{t+\Delta t}_{t}S^{vol}_{MN}\delta\,{}^{t+\Delta t}_{t}E_{MN}d\Omega + \int_{\Omega_t} (1-D)\,{}^{t+\Delta t}_{t}S^{dev}_{MN}\delta\,{}^{t+\Delta t}_{t}E_{MN}d\Omega \\
&= \int_{\Gamma_t} \bar{T}^{0}_{I}\delta u_i d\Gamma + \int_{\Omega_t} {}^{t}\rho b_i \delta u_i d\Omega - \int_{\Omega_t} {}^{t}\rho \ddot{u}_i \delta u_i d\Omega \\
&+ \int_{\Omega_t} (1-D)\,{}^{t+\Delta t}_{t}S^{Piezo}_{MN}\delta\,{}^{t+\Delta t}_{t}E_{MN}d\Omega + \int_{\Omega_t} {}^{t+\Delta t}_{t}S^{Maxwell}_{MN}\delta\,{}^{t+\Delta t}_{t}E_{MN}d\Omega
\end{aligned} \tag{3.36}$$

The density and the body force are assumed to remain unchanged in the presence of damage. The traction boundary conditions with damage is given as:

$${}^{t+\Delta t}_{t}T_I = \left[{}^{t+\Delta t}_{t}P^{vol}_{iJ} + (1-D)\,{}^{t+\Delta t}_{t}P^{dev}_{IJ}\right]{}^{t}N_J = \bar{T}^{t}_{I} \quad \text{on } \Gamma_t$$

FE Implementation of the Continuum Damage Model

The finite element implementation of the continuum damage model is incrementally done in the material constitutive framework, where stresses and all state variables are evaluated at each integration point for the given strain increment. With all state variables, including the stress ${}^{t}_{t}S_{IJ} = {}^{t}\sigma_{ij}$, damage parameter ${}^{t}D$ known for the reference configuration at time $t = t$, the mechanical field variables are updated for a given displacement increment ΔU_I. Essential steps in the implementation of the damage model are given below.

1. *Initialization:* Assuming no damage evolution at time $t = t + \Delta t$, evaluate the incremental values for the strain driven process.

$${}^{t+\Delta t}_{0}F_{IJ} = {}^{t}_{0}F_{IJ} + \frac{\partial \Delta U_I}{\partial\,{}^{0}X_j}, \quad {}^{t+\Delta t}_{0}C_{IJ} = {}^{t+\Delta t}_{0}F_{IK}\,{}^{t+\Delta t}_{0}F_{JK}, \quad {}^{t+\Delta t}_{0}J = det\left({}^{t+\Delta t}_{0}F_{IJ}\right) \tag{3.37}$$

   From equation (3.37), the strain decomposition for volume preserved part is given as:

$${}^{t+\Delta t}_{0}\overline{F}_{IJ} = {}^{t+\Delta t}_{0}J^{-\frac{1}{3}}\,{}^{t+\Delta t}_{0}F_{IJ}, \quad {}^{t+\Delta t}_{0}\overline{C}_{IJ} = {}^{t+\Delta t}_{0}\overline{F}_{IK}\,{}^{t+\Delta t}_{0}\overline{F}_{JK} \tag{3.38}$$

2. *Predictor Algorithm for Damage Evolution:* Calculate the history variables for the damage model from section 3.1.1 as:

$${}^{t+\Delta t}\Xi^{max} = max\left\{{}^{t+\Delta t}\Xi^{trial}, {}^{t}\Xi^{max}\right\} \tag{3.39}$$

where

$$ {}^{t+\Delta t}\Xi^{trial} = \sqrt{2\,{}^{t+\Delta t}\Psi_0^{dev}} \quad \text{and} \quad {}^{t+\Delta t}\Psi_0^{dev} = \Psi_0^{dev}\left({}^{t+\Delta t}_{0}\overline{C}_{IJ}\right) \tag{3.40} $$

If ${}^{t+\Delta t}\Xi^{max} = {}^{t}\Xi^{max}$, damage does not evolve in the current increment. Proceed to step 3 with no damage evolution and:

$$ {}^{t+\Delta t}D = {}^{t}D \tag{3.41} $$

Else, if ${}^{t+\Delta t}\Xi^{max} = {}^{t+\Delta t}\Xi^{trial}$, damage will evolve in the current increment. The damage parameter is updated using equation (3.15) as:

$$ {}^{t+\Delta t}D = {}^{t}D - \frac{g'}{{}^{t+\Delta t}\Xi^{max}} \frac{\partial \Psi_0^{dev}}{\partial E_{IJ}} \Delta E_{IJ} \tag{3.42} $$

Proceed to step 3 with the updated damage parameter.

3. *Update Tangent Stiffness Matrix and Piezoelectric Coupling Coefficient:* For evolving damage, the tangent stiffness tensor of the deviatoric stress is calculated with the updated damage parameter as:

$$ {}_{t}C_{IJKL}^{dev} = g({}^{t+\Delta t}\Xi^{max}) \frac{\partial \Psi_0^{dev}}{\partial E_{IJ} \partial E_{KL}} + \frac{g'}{{}^{t+\Delta t}\Xi^{max}} \frac{\partial \Psi_0^{dev}}{\partial E_{IJ}} \frac{\partial \Psi_0^{dev}}{\partial E_{KL}} \tag{3.43} $$

The piezoelectric coupling coefficient is updated as:

$$ \hat{\mathscr{P}}_{IPQ} = g({}^{t+\Delta t}\Xi^{max})\, \hat{\mathscr{P}}_{IPQ} \tag{3.44} $$

If the damage evolution criterion is not met, the tangent modulus of the deviatoric stress is calculated as:

$$ {}_{t}C_{IJKL}^{dev} = g({}^{t+\Delta t}\Xi^{max}) \frac{\partial \Psi_0^{dev}}{\partial E_{IJ} \partial E_{KL}} \tag{3.45} $$

and the piezoelectric coefficient is:

$$ \hat{\mathscr{P}}_{IPQ} = g({}^{t+\Delta t}\Xi^{max})\, \hat{\mathscr{P}}_{IPQ} \tag{3.46} $$

This step is bypassed if the damage model is not activated.

3.2.2 Electric Field for Piezoelectric Material with Damage

For each step, the governing and constitutive equations of the transient electric field problem in equations (3.20) and (3.27b) are solved in the reference configuration $\Omega_0 = \Omega(t = 0)$. The weak form of the electric field problem is derived using the Hamilton's principle [18, 24] that involves minimization of the action functional S over the time range, defined in terms of the time-dependent Lagrangian density $\mathscr{L}$ in the reference domain. The minimization condition is expressed as:

$$ \delta S = \delta \int_{t_1}^{t_2} \int_{\Omega_0} \mathscr{L}\, d\Omega_0 dt = 0 \tag{3.47} $$

where the Lagrangian density in the reference configuration $\mathscr{L}$, is given as:

$$\mathscr{L} = \frac{\varepsilon J}{2} C_{JK}^{-1} E_J E_K + (1-D)\hat{\mathscr{P}}_{IJK} E_{IJ} E_K \tag{3.48}$$

Here E_I is written in terms of the scalar potential in equation (3.18). Setting the variation of the action functional S with respect to Φ to zero in equation (3.47) yields:

$$S_{,\Phi}[\delta\Phi] = \int_{t_1}^{t_2} \int_{\Omega_0} \mathscr{L}_{,\Phi}[\delta\Phi]\Omega_0 dt = 0 \tag{3.49}$$

Since t_1 and t_2 are arbitrary, equation (3.49) leads to the condition $\int_{\Omega_0} \mathscr{L}_{,\Phi}[\delta\Phi] dV_0 = 0$. Substituting equation (3.18) in this condition, the weak form of the electric problem at time $t+\Delta t$ is obtained as:

$$\begin{aligned} &\int_{\Gamma_0} N_I \left[\varepsilon\, {}^{t+\Delta t}J\, {}^{t+\Delta t}C_{IJ}^{-1}\, {}^{t+\Delta t}_{t}(-\Phi_{,J}) - (1-{}^{t+\Delta t}D)\hat{\mathscr{P}}_{IPQ}\, {}^{t+\Delta t}_{t}E_{PQ} \right] \delta\Phi d\Gamma \\ &- \int_{\Omega_0} \left[\varepsilon J C_{IJ}^{-1} E_J - (1-D)\hat{\mathscr{P}}_{IPQ} E_{PQ} \right] \delta\Phi_{,I}\, d\Omega = 0 \end{aligned} \tag{3.50}$$

For Dirichlet boundary conditions on Γ_1, where $\Phi = \Phi_0$ or $\Phi = 0$ representing grounded boundary, $\delta\Phi = 0$ in equation (3.50). Another common boundary condition which affects the boundary term of equation (3.50) is $N_I D_I = 0$, where D_I is defined in equation (3.27b). This boundary condition is applied at a dielectric-dielectric interface, when one of the dielectric constants is large compared to the other, such as at an air-dielectric interface. The boundary condition of current injection into the structure at a free boundary is not incorporated, since the conductivity is significantly small to induce any conducting current or free charge current density. Damage evolution does not affect the Dirichlet boundary condition when $\delta\Phi = 0$ or the homogeneous Neumann boundary condition.

FE Implementation of the Coupled Finite Deformation Dynamics and Electric Field for Piezoelectric Material

For piezoelectric material relations in the finite deformation setting, the second Piola Kirchhoff stress admits additional terms that correspond to the piezoelectric effect and Maxwell stress. In the updated Lagrangian formulation, the stress at $t = t+\Delta t$ is evaluated from known values in the reference configuration at time t as:

$${}^{t+\Delta t}_{t}S_{IJ} = {}^{t}_{t}S_{IJ} + \Delta S_{IJ} = {}^{t}\sigma_{ij} + \Delta S_{IJ} \tag{3.51}$$

with known ${}^{t}\sigma_{ij}$. The increment of the second Piola-Kirchoff stress ΔS_{IJ} is additively decomposed in accordance with equation (3.29) as:

$$\Delta S_{IJ} = \Delta S_{IJ}^{vol} + \Delta S_{IJ}^{dev} + \Delta S_{IJ}^{Piezo} + \Delta S_{IJ}^{Maxwell} \tag{3.52}$$

Using equations (3.27a) and (3.30), the increment of the second Piola-Kirchoff stress can be expressed in terms of increments of the strain tensor ΔE_{IJ} and the electric field ΔE_K as:

$$\Delta S_{IJ} = {}_{t}C_{IJKL}\Delta E_{KL} + {}_{t}\tilde{\mathscr{P}}_{SIJ}\Delta E_S = \left[{}_{t}C_{IJKL}^{vol} + {}_{t}C_{IJKL}^{dev} + {}_{t}C_{IJKL}^{Maxwell} \right] \Delta E_{KL} + {}_{t}\tilde{\mathscr{P}}_{SIJ}\Delta E_S \tag{3.53}$$

where the different tangent stiffness components are given as:

$$ {}_tC^{vol}_{IJKL} = 2\frac{\partial S^{vol}_{IJ}}{\partial C_{KL}} = 4\frac{\partial^2 \Psi^{vol}}{\partial C_{IJ}\partial C_{KL}} \tag{3.54a} $$

$$ {}_tC^{dev}_{IJKL} = 2\frac{\partial S^{dev}_{IJ}}{\partial C_{KL}} = 4\frac{\partial^2 \Psi^{dev}}{\partial C_{IJ}\partial C_{KL}} \tag{3.54b} $$

$$ {}_tC^{Maxwell}_{IJKL} = 2\frac{\partial S^{Maxwell}_{IJ}}{\partial C_{KL}} \tag{3.54c} $$

Additionally the coupling coefficient is expressed as:

$$ {}_t\tilde{\mathscr{P}}_{SIJ} = \mathscr{H}^{Maxwell}_{SIJ} - \hat{\mathscr{P}}_{SIJ}, \quad \text{where} \quad \mathscr{H}^{Maxwell}_{SIJ} = \frac{\partial S^{Maxwell}_{IJ}}{\partial E_S} \tag{3.55} $$

Explicit derivations of $C^{Maxwell}_{IJKL}$ and $\mathscr{H}^{Maxwell}_{SIJ}$ are presented in 3.A.

The incremental solution process requires linearization of the nonlinear relations in the above weak forms. Using the forward Euler time integration, the increment of the electric field is evaluated as:

$$ \Delta E_I = {}^{t+\Delta t}E_I - {}^tE_I = \left({}^t\Phi_{,I} - {}^{t+\Delta t}\Phi_{,I}\right) \approx -\Delta t\,{}^t\dot{\Phi}_{,I} \tag{3.56} $$

The first variation of the Green-Lagrange strain tensor is given as:

$$ \delta\,{}^{t+\Delta t}_{t}E_{IJ} = \delta\Delta e_{IJ} + \delta\Delta\eta_{IJ} \tag{3.57} $$

where

$$ \Delta e_{IJ} = \frac{1}{2}\left(\frac{\partial \Delta u_I}{\partial {}^tX_J} + \frac{\partial \Delta u_J}{\partial {}^tX_I} + \frac{\partial {}^tu_I}{\partial {}^tX_J}\frac{\partial \Delta u_J}{\partial {}^tX_I} + \frac{\partial {}^tu_J}{\partial {}^tX_I}\frac{\partial \Delta u_I}{\partial {}^tX_J}\right) \quad \text{and} \quad \Delta\eta_{IJ} = \frac{1}{2}\frac{\partial \Delta u_I}{\partial {}^tX_J}\frac{\partial \Delta u_J}{\partial {}^tX_I} \tag{3.58} $$

are the linear and nonlinear components of the increment of the strain increment. Using the linearized relations in equation (3.57), the second Piola Kirchhoff stress increment for the coupled system is calculated as:

$$ \Delta S_{IJ} \approx {}_tC_{IJKL}\Delta e_{KL} - {}_t\tilde{\mathscr{P}}_{SIJ}\Delta t\,{}^t\dot{\Phi}_{,S} \tag{3.59} $$

The weak form of the mechanical field for the piezoelectric materials is then derived from equation (3.36) as:

$$ \begin{aligned} &\int_{\Omega_t} {}^tC_{MNPQ}\Delta e_{MN}\delta\Delta e_{MN}d\Omega_t + \int_{\Omega_t} {}^t\sigma_{mn}\delta\Delta\eta_{MN}d\Omega - \int_{\Omega_t} {}_t\tilde{\mathscr{P}}_{SMN}\Delta\eta_{MN}d\Omega \\ &= \int_{\Gamma_t} \bar{T}^0_I\delta u_i d\Gamma + \int_{\Omega_t} {}^t\rho b_i\delta u_i d\Omega - \int_{\Omega_t} {}^t\rho\ddot{u}_i\delta u_i d\Omega - \int_{\Omega_t} {}^t\sigma_{mn}\delta\Delta e_{MN}d\Omega + \int_{\Omega_t} {}_t\tilde{\mathscr{P}}_{SMN}\Delta e_{MN}d\Omega \end{aligned} \tag{3.60} $$

Once the damage model is triggered, the tangent stiffness matrix corresponding to the deviatoric second Piola Kirchhoff stress ${}_tC^{dev}_{IJKL}$ and the piezoelectric coupling term ${}_t\tilde{\mathscr{P}}_{SIJ}$ are governed by

equations (3.43) and (3.44) for evolving damage, and by equations (3.45) and (3.46) for non-evolving damage.

For the electric field in the total Lagrangian formulation, the weak form in equation (3.50) is expressed as:

$$\begin{aligned}&\int_{\Gamma_0} {}^0N_I \left(\varepsilon\, {}^{t+\Delta t}_0J\, {}^{t+\Delta t}_0C^{-1}_{IJ}\, {}^{t+\Delta t}_0E_J - \hat{\mathscr{P}}_{IPQ}\, {}^{t+\Delta t}_0E_{PQ}\right)\delta\Phi d\Gamma \\ &-\int_{\Omega_0}\left(\varepsilon\, {}^{t+\Delta t}_0J\, {}^{t+\Delta t}_0C^{-1}_{IJ}\, {}^{t+\Delta t}_0E_J - \hat{\mathscr{P}}_{IPQ}\, {}^{t+\Delta t}_0E_{PQ}\right)\delta\Phi_{,I}\, d\Omega = 0\end{aligned} \tag{3.61}$$

Equation (3.61) may be written in terms of electric scalar potential as:

$$\begin{aligned}&\int_{\Gamma_0} {}^0N_I \left(\varepsilon\, {}^{t+\Delta t}_0J\, {}^{t+\Delta t}_0C^{-1}_{IJ}\, {}^{t+\Delta t}\Phi_{,J} + \hat{\mathscr{P}}_{IPQ}\, {}^{t+\Delta t}_0E_{PQ}\right)\delta\Phi d\Gamma \\ &-\int_{\Omega_0}\left(\varepsilon\, {}^{t+\Delta t}_0J\, {}^{t+\Delta t}_0C^{-1}_{IJ}\, {}^{t+\Delta t}\Phi_{,J} + \hat{\mathscr{P}}_{IPQ}\, {}^{t+\Delta t}_0E_{PQ}\right)\delta\Phi_{,I}\, d\Omega = 0\end{aligned} \tag{3.62}$$

In the staggered solution method, the mechanical field variables at time $t+\Delta t$ are first evaluated. Relevant variables are subsequently passed on for solution of the electric field. The piezoelectric coupling term is changed according to equation (3.44) or equation (3.46) respectively, depending on whether or not the damage model is activated.

3.3 Numerical Results with the Coupled Dynamics and Electric Field Model for Piezoelectric Material

Two numerical examples are considered in this section for validating the coupled mechanical and piezoelectric model and (ME-PE) code. The first is a validation test for the ME-PE model by comparing with an analytical solution. The second example involves comparison of ME-PE simulation results with those from simulations by the commercial code [1] for an auxetic material.

3.3.1 Validation of ME-PE Model for a Bimorph Beam

The ME-PE code for the piezoelectric material is validated by simulating a bimorph beam that has been analyzed in [36, 58]. The analytical solution for small deformation piezoelectricity has been derived in [54].

The piezoelectric series bimorph beam is made of the upper and lower piezoelectric elements, for which the electric field driving the bimorph is generated by the top and bottom electrodes, as shown in figure 3.1(a). The upper element has anti-parallel polarization while the lower element has its polarization parallel to the electric field. The beam is clamped at the end S_2 and is free at the other end, allowing bending under an applied electric voltage. A voltage $V = 1V$ is applied between the top and bottom surfaces and the interface between the upper and lower parts is grounded. The material is neo-Hookean, with the Lam*é* constants in equation (3.8) set to $\lambda = 0$,

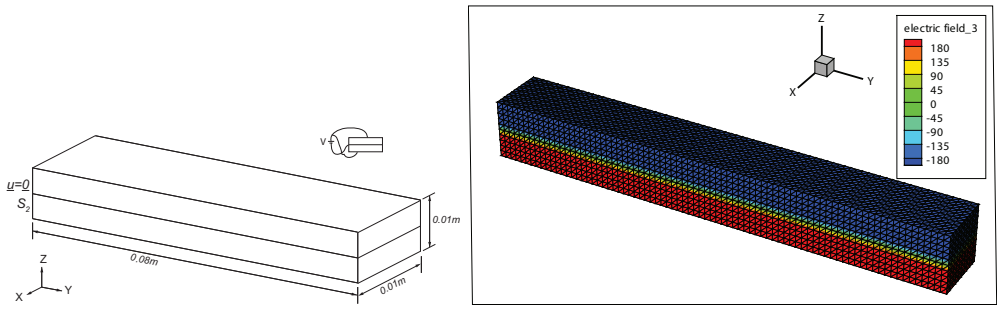

(a) (b)

Figure 3.1: Simulation of a piezoelectric bimorph beam: (a) geometry and boundary conditions of the beam, and (b) the simulated electric field in z-direction.

$\mu = 45$GPa. The piezoelectric coupling constant is $\hat{\mathscr{P}}_{311} = \hat{\mathscr{P}}_{322} = 0.0460\text{C/m}^2$. The permittivity is $\varepsilon_{11} = \varepsilon_{22} = \varepsilon_{33} = 0.1062 \times 10^{-9}$F/m. The contour plot of the electric field in z-direction is shown in figure 3.1 (b). The electric field induced stresses deform the beam. For small deformation, geometric and material nonlinearity are not significant. The analytical solution of z-direction deflection as a function of position in the x direction has been derived in [54] as:

$$u_z = 3\frac{\hat{\mathscr{P}}_{31}V}{Eh^2}x^2 \tag{3.63}$$

where E is the Young's modulus that can be derived from the Lam*é* constants for small deformation. The deflection of the beam along the x-direction is plotted in figure 3.2 and compared with the analytical solution. The agreement is excellent.

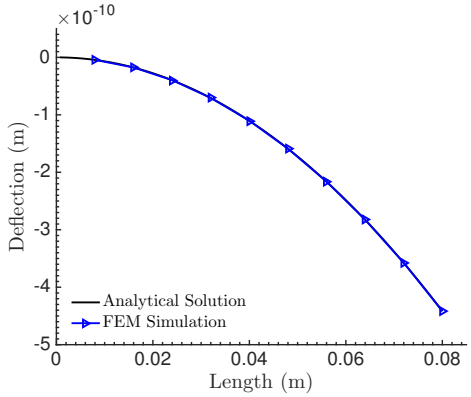

Figure 3.2: Comparing the simulated z-deflection of the bimorph beam along the x-direction with the analytical solution.

3.3.2 Simulations for an Auxetic Material and Comparing with ABAQUS

Negative Poisson's ratio for auxetic materials have been experimentally and numerically studied in [51] using elastic sheets with embedded periodic arrays of elongated cuts. In [51] it has been shown

that the Kagome-cut and square-cut of certain auxetic structures, shown in figure 3.3(a), can achieve negative Poisson's ratio. The minimum Poisson's ratio has been obtained at an angle $\theta = 90^\circ$. The square-cut pattern shown in figure 3.3 is simulated in this study to validate the coupled piezoelectric model.

The 3D model in figure 3.3(b) has dimensions $L_x = L_y = 525$mm in the x- and y-directions and a thickness of $t = 100$mm. The size of the undeformed representative volume element (RVE) analyzed, is 10mm $\times$ 10mm, as shown in figure 3.3(b). The simulating angle is $\theta = 90^\circ$ and the length of the cut is $l_{cut} = 40$mm. Boundary conditions for mechanical field are $u_x = 0,\ u_y = 0$ at $x = 0, y = 0$ and u_y is constrained for all other locations of $y = 0$. A uniform loading of 100MPa is applied at $y = L_y$. For the electric field, the structure is grounded at $x = 0, y = 0$. The material properties are chosen as $\lambda = 1.907 \times 10^9$Pa, $\mu = 3.390 \times 10^9$Pa, permittivity $\varepsilon_{11} = \varepsilon_{22} = \varepsilon_{33} = 1.06 \times 10^{-10}$ F/m and the piezoelectric coupling coefficients are $\hat{\mathscr{P}}_{111} = 0.2034$C/m^2 and $\hat{\mathscr{P}}_{122} = -0.2034$C/m^2.

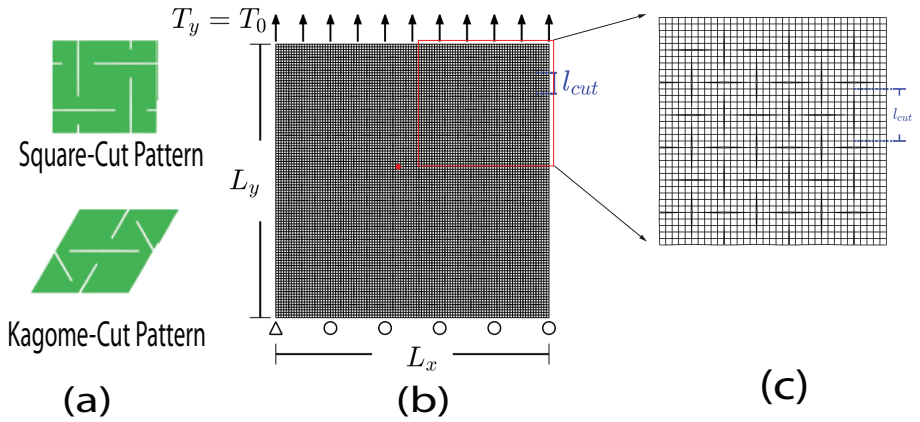

Figure 3.3: (a) Representative volume elements of the square-cut and Kagome-cut patterns analyzed; (b) the 10×10 mesh, and (c) zoom-in view for the square-cut pattern of the auxetic structure with cut angle $\theta = 90^\circ$.

Simulations with the coupled mechanical-electric (ME-PE) code for the piezoelectric material are compared with those by the commercial code [1], which can simulate only small deformation with a linear elastic model. The effective Young's modulus is $E = \frac{\mu(3\lambda+2\mu)}{\lambda+\mu} = 8$GPa and Poisson's ratio $\nu = \frac{\lambda}{2(\lambda+\mu)} = 0.18$ for the ABAQUS study. All the other material properties remain the same. Results of simulations by the ABAQUS and ME-PE code are given in table 3.1. The small discrepancy is due to the difference in small and finite deformation formulations in the two programs.

The convergence of the staggered coupling scheme for piezo-electricity in the ME-PE model and code is also studied in this example. Results at a node labeled with the red dot in figure 3.3 at a location $x = 235mm$ and $y = 290mm$ are studied for different loading conditions. Two different

	ABAQUS		ME-PE Code	
Variable	minimum value	maximum value	minimum value	maximum value
Φ (MV)	-2.8	10.4	-2.8	11.6
ε_{11}	-0.166	0.133	-0.08	0.135
ε_{22}	-0.057	0.191	-0.051	0.196
$u_{y_{max}}$(mm)	594.5		579.91	

Table 3.1: Comparison of results for the square-cut pattern RVE model by ABAQUS (small deformation) and the ME-PE code (finite deformation).

solution approaches are considered. In the first approach, the loading is incremented in each time step during which, the staggered solver is applied. Every time step involves solving the mechanical problem first followed by the electric problem. The solutions are obtained with 10, 20 and 40 time steps. In the second scheme, a larger load is applied in each step. For each load increment, the coupled ME-PE solution process is further discretized into 5 sub-steps for which an iterative solver is activated till convergence. Figure 3.4 shows the convergence of the mechanical traction, electric potential Φ and Green-Lagrange strain in the y-direction E_{22} by the two approaches as a function of the steps. For the first approach, the smaller increments for larger number of steps yield more accurate results. For the second approach the iteration with large load steps require larger number of iterations to converge. The electric potential Φ and Green-Lagrange strain E_{22} yield the same convergent results with both the approaches. The results show that the staggered method can achieve accurate result as long as the time step is well-controlled.

3.4 Developing a Piezoelectric Damage Sensor using the Coupled Piezoelectric Model

A virtual piezoelectric damage sensor is proposed in this section, in which the electric field may be used as an indicator of damage in the substrate. Damage due to mechanical loading degrades both the stiffness and piezoelectric coupling coefficients, which alters the electric field for a given mechanical load. The difference in the electric field ΔE_I between damaged and undamaged material states can be correlated to the deviatoric strain energy density Ψ^{dev} from which the damage state can be estimated. It is of interest to develop a function correlating the electric field difference to the damage, its rate etc., e.g. $\Delta E_I = f(D, \dot{D}, \cdots)$, as a virtual sensor.

3.4.1 Calibrating an Electric Field-based Damage Indicator Function

For the correlation function, it is important to postulate two conjectures through numerical studies.

- The electric field in the damaged structure is different than that in the undamaged structure for the same mechanical and electric loading and boundary conditions.
- The deviatoric strain energy density Ψ^{dev} can be correlated to the damage parameter D.

Numerical studies with the finite deformation, piezoelectric model and (ME-PE) code is used to

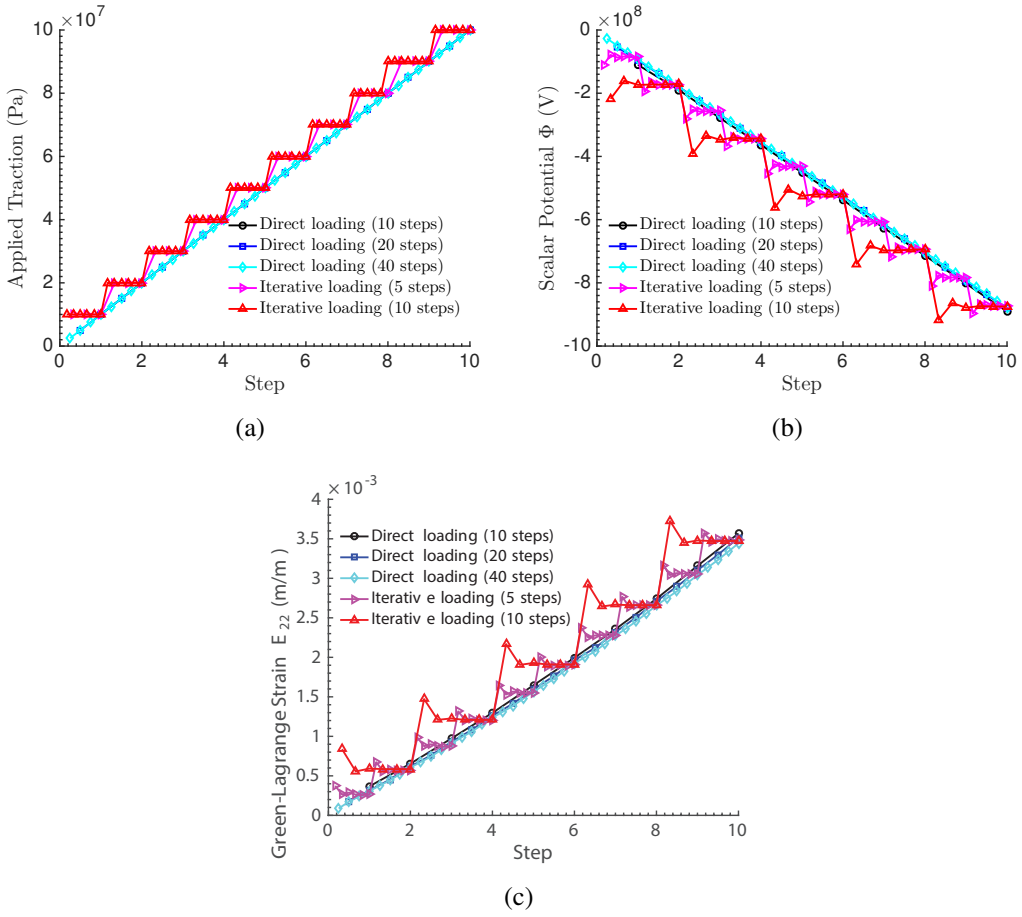

Figure 3.4: Different loading schemes and solution approaches for convergence study: Convergence of (a) the mechanical traction, (b) the electric potential Φ; and (c) the Green-Lagrange strain E_{22}, for different loading schemes.

establish the correlation function. As shown in figure 3.5, a thin rectangular plate with a notch in the middle is simulated to explore the connection between electric and damage fields. Dimensions of the specimen in figure 3.5(a) are $H = 0.01$m, $L = 0.05$m, $l = 0.019$m, $r = 0.003$m, $R = 0.007$m and $\theta = 0.6435$ radians. The thickness of the model is $t = 0.002$m. The 3D finite element mesh of the model is shown in figure 3.5(b). The notched geometry leads to a nonuniform stress field and a spatial distribution of damage in the $x-y$ plane.

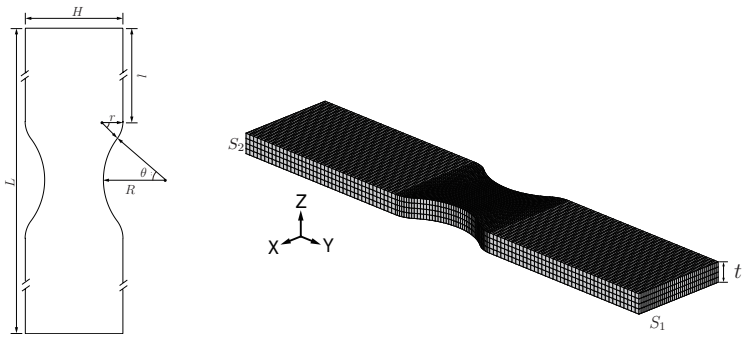

(a) (b)

Figure 3.5: (a) Two dimensional schematic of the thin plate with a notch, and (b) 3D model and mesh of the plate.

Sensitivity analysis of the damage parameter D is conducted using simulations with the ME-PE code. Mechanical properties of the structure are: $\lambda = 0$, $\mu = 35$GPa and $\nu = 0$. The piezoelectric constant is $\hat{\mathscr{P}}_{222} = -0.001\text{C/m}^2$ and the permittivity is $\varepsilon = 1.0$F/m. The plate is fixed at one end i.e. $\boldsymbol{u} = 0$ on the surface of S_2. The other end S_1 is subjected to a y-directional uniaxial strain load $u_y = 0.0005t$ that is applied incrementally with time. For the piezoelectric problem, the boundary condition is set as: $\Phi = 0$ at $y = 0.025$m.

Since the plate is thin, variation of solutions along z-direction is not significant and the analysis is focused on the middle layer $z = 0.001$. Simulations are conducted with the damage parameter set to $D = 0.0,\ 0.05,\ 0.1,\ 0.15$ and 0.2 respectively and $\dot{D} = 0$. The undamaged model with $D = 0.0$ is serves as the reference for the electric field. Key variables such as the electric field, Green-Lagrange strain, deviatoric strain energy are recorded at the nodal points in the rectangular region $0.0048\text{m} \leq x \leq 0.0052$m, $0.022\text{m} \leq y \leq 0.028$m and $z = 0.001$m. The difference of the electric field between the undamaged and four damaged specimens, as well as the deviatoric strain energy at each integration point, are evaluated at each incremental time step. The difference in the electric field is plotted as a function of the strain energy density for different damage values in figure 3.6.

Damage indicator function in terms of damage variables

The difference of the electric field is seen to have a linear trend with respect to the strain energy for each damage state. The simulation data is used to calibrate relationship between the variables

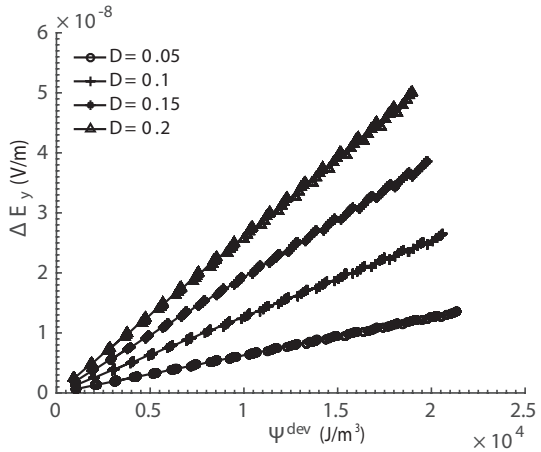

Figure 3.6: Difference in the electric field between the undamaged and damaged models as a function of the strain energy density for different damage parameters.

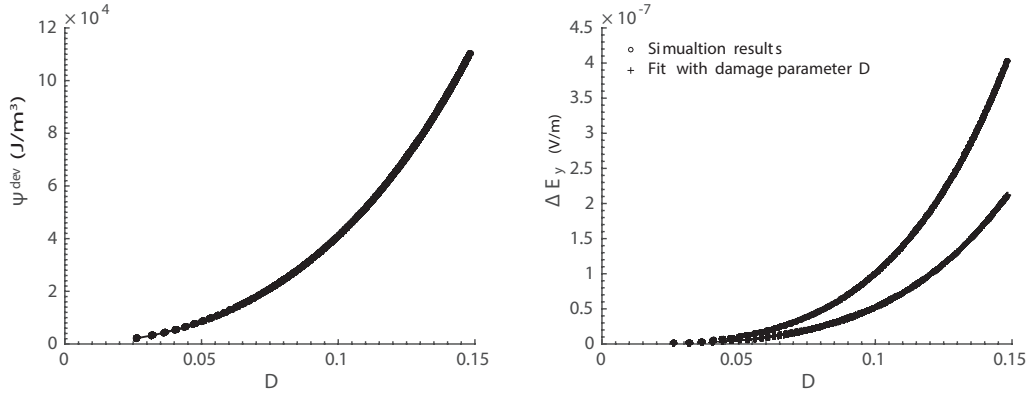

Figure 3.7: (a) Relation between the damage parameter D and deviatoric energy Ψ^{dev} for the uniaxially loaded specimen and (b) comparing the $\Delta E_y - d$ plot from the calibrated form in equation (3.66) with direct numerical simulations.

as:

$$\Delta E_y = f(D)\Psi^{dev} \quad \text{such that} \quad f(D) = 3.408\times10^{-12}D^2 + 12.39\times10^{-12}D \tag{3.64}$$

Here $f(D)$ corresponds to the slope of the plots in figure 3.6. To explore the relationship between Ψ^{dev} and the damage parameter D, simulations are conducted with damage evolution and also without damage. Damage parameters in equation (3.14) are chosen to be: $\alpha = 600$ and $\beta = 0.5$. Numerical analysis with and without damage model is simulated. The deviatoric strain energy Ψ^{dev} at each integration point and the damage parameter are well correlated as shown in figure 3.7(a). The relation between these variables is expressed by a polynomial based indicator function as:

$$\Psi^{dev} = g(D) = 7.146\times10^{7}D^4 + 3.587\times10^{6}D^2 - 1.873\times10^{4}D \tag{3.65}$$

In the absence of dependence on the rate of damage $\dot{D}$, the difference in the elastic field is obtained by combining equations (3.64) and (3.65) as:

$$\Delta E_y = \left(3.408\times10^{-12}D^2 + 12.39\times10^{-12}D\right)\times\left(7.146\times10^{7}D^4 + 3.587\times10^{6}D^2 - 1.873\times10^{4}D\right) \tag{3.66}$$

A comparison of the $\Delta E_y - D$ plot from the calibrated form in equation (3.66) with direct numerical simulations in figure 3.7(b) shows that the dependence on the damage state alone is not able to provide a good indicator function. It is postulated that the rate of damage is also an important parameter in this indicator function relation. Including the variable $\dot{D}$ in a modified calibrated expression leads to the indicator function as:

$$\begin{aligned}\Delta E_y = &-2.883\times10^{-6}D + 2.399\times10^{-6}D\dot{D} + 7.285\times10^{-5}D^2 + 1.087\times10^{-9}\dot{D}^2 \\ &- 3.749\times10^{-5}D^2\dot{D} - 7.285\times10^{-7}D\dot{D}^2 - 5.714\times10^{-4}D^3 - 6.565\times10^{-11}\dot{D}^4 \\ &+ 7.572\times10^{-8}D\dot{D}^3 + 4.946\times10^{-6}D^2\dot{D}^2 + 1.576\times10^{-4}D^3\dot{D} + 2.2\times10^{-3}D^4\end{aligned} \tag{3.67}$$

The corresponding plot of the $\Delta E_y - D$ from equation (3.67) in figure 3.8(a) matches the results from direction numerical simulations very well. The error plot in figure 3.8(b) shows that the error is bounded to within 3%. Thus it may be concluded that both D and $\dot{D}$ are needed as independent variables in the expression for the damage indicator function.

Dependence of damage indicator function on material properties

It is important to investigate the effect of material properties on the damage indicator function in equation (3.67). Two properties, viz. the elastic stiffness $E = \frac{\mu(3\lambda+2\mu)}{\lambda+\mu}$ and the piezoelectric coupling coefficient $\hat{\mathscr{P}}_{SIJ}$ are studied. For the mechanical property E, three values are chosen for ME-PE simulations as:

- Modulus I: $E = 70$MPa
- Modulus II: $E = 35$MPa
- Modulus III: $E = 7$MPa

The corresponding electric field difference ΔE_y is plotted as a function of the damage parameter D at nodes in the region $0.0048 \le x \le 0.0052$, $0.022 \le y \le 0.028$ and $z = 0.001$, for the three moduli.

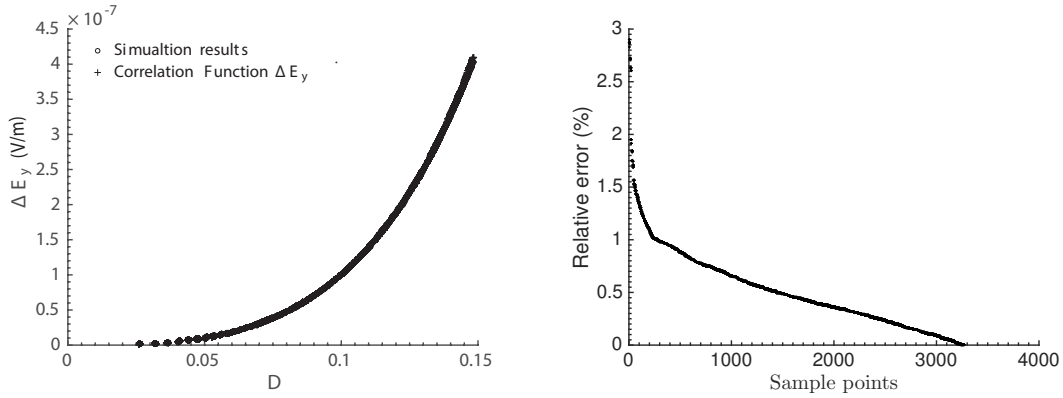

(a) (b)

Figure 3.8: (a) Comparing the $\Delta E_y - d$ plot from the calibrated form $\Delta E_y(D,\dot{D})$ in equation (3.67) with direct numerical simulations, (b) relative error of the calibrated indicator function with the direct simulation results.

The results are shown in figure 3.9(a), which shows the dependence on the stiffness. When the ΔE_y values are normalized by the modulus, the plots in figure 3.9(b) are seen to plots merge indicating a linear relations between ΔE_y and E. Specifically ΔE_{y_I} is multiplied by 1, $\Delta E_{y_{II}}$ is multiplied by $\frac{E_{II}}{E_I} = 0.5$ and $\Delta E_{y_{III}}$ is multiplied by $\frac{E_{III}}{E_I} = 0.1$ in figure 3.9(b). This is a consequence of the fact that a larger elastic modulus results in smaller damage.

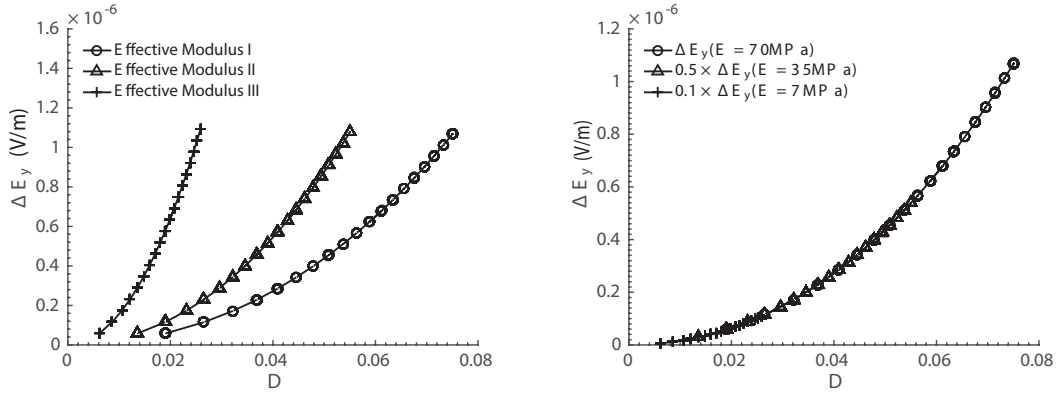

(a) (b)

Figure 3.9: (a) $\Delta E_y - D$ plot for materials with different elastic moduli, and (b) plot of ΔE_y normalized by the elastic moduli.

Next the dependence of the damage indicator function in equation (3.67) on the piezoelectric coupling constant $\hat{\mathscr{P}}_{SIJ}$ is investigated. for the piezoelectric property sensitivity study, three values are chosen for the coupling constant, viz.:

- Piezo I: $\hat{\mathscr{P}}_{222} = 0.001$

- Piezo II: $\hat{\mathscr{P}}_{222} = 0.002$
- Piezo III: $\hat{\mathscr{P}}_{222} = 0.004$

For the same elastic moduli, the mechanical and damage response are the same. However, the value of ΔE_y changes with the coupling coefficient $\hat{\mathscr{P}}_{222}$. A smaller value of $\hat{\mathscr{P}}_{22}$ yields a weaker coupling between the mechanical and eclectic fields with a smaller ΔE_y.

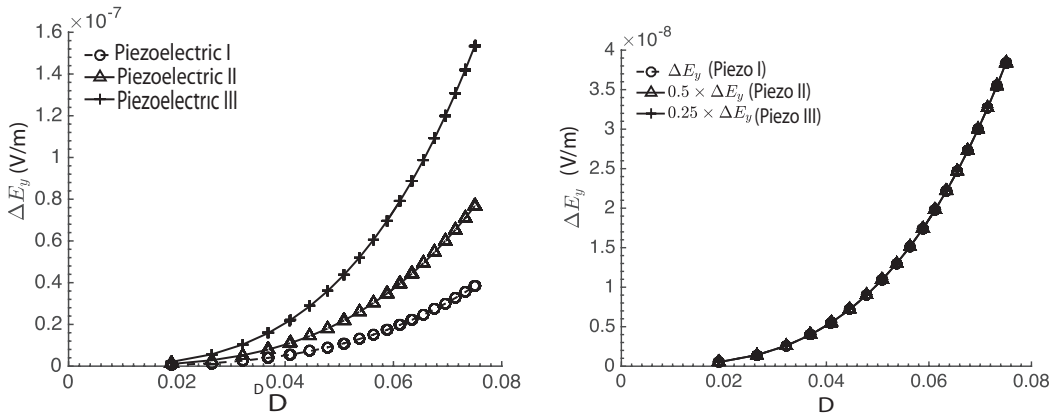

Figure 3.10: (a) $\Delta E_y - D$ plot for materials with different piezoelectric coupling constants, and (b) plot of ΔE_y normalized by the piezoelectric coupling constant.

Again the electric field difference ΔE_y is plotted as a function of D for the three piezoelectric coupling constants in figure 3.10(a), exhibiting material dependence. Upon normalizing ΔE_y by the coupling constants, i.e. multiplying ΔE_{y_I} by 1, $\Delta E_{y_{II}}$ by $\frac{\hat{\mathscr{P}}_I}{\hat{\mathscr{P}}_{II}} = 0.5$ and $\Delta E_{y_{III}}$ by $\frac{\hat{\mathscr{P}}_I}{\hat{\mathscr{P}}_{III}} = 0.25$, a unified plot is seen in figure 3.10(b). Again, this points to the linear relation between ΔE_y and $\hat{\mathscr{P}}_{222}$.

In conclusion, the material property-based sensitivity study indicates that $\Delta E_y \propto \frac{1}{E}$ and $\propto \hat{\mathscr{P}}_{222}$. Combining this with the relation in equation (3.67), the electric field-based damage indicator function is expressed as:

$$\Delta E_y = \frac{E^{ref}}{\hat{\mathscr{P}}^{ref}_{222}} \times \frac{\hat{\mathscr{P}}_{222}}{E} \Delta E_y^{ref} = 10^9 \frac{\hat{\mathscr{P}}_{222}}{E} \Delta E_y^{ref} \tag{3.68}$$

where ΔE_y^{ref} is the reference function in equation (3.67).

3.4.2 Testing the Damage Indicator Function for Stretchable Piezoelectric Conductors

Stretchable electronic structures are increasingly gaining popularity in a wide variety of sensor applications. A similar structural concept of a stretchable piezoelectric conductor is explored in this study with the coupled piezoelectric model. The numerical model of the stretchable piezoelectric

conductor follows that of a serpentine structure discussed in [27]. A schematic of the serpentine structure and the three-dimensional mesh is shown in figure 3.11. Pertinent dimensions of the structure are: $w = 0.4$m, $\alpha = 15^\circ$, $R = 2$m, $l = 2$m. Mechanical properties of the compressible neo-Hookean material are: $\lambda = 0$ and $\mu = 35$GPa. The piezoelectric constant is $\hat{\mathscr{P}}_{211} = -0.001$, which couples the deformation in x-direction and the electric field in y-direction. The permittivity is $\varepsilon = 1.0$.

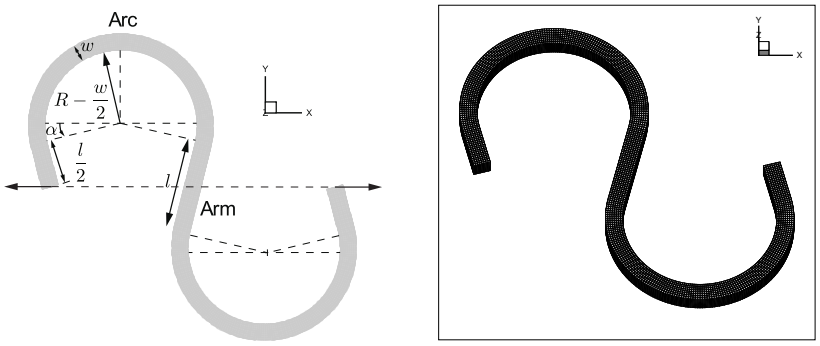

(a) (b)

Figure 3.11: (a) A two-dimensional schematic with dimensions of a stretchable serpentine piezoelectric conductor; (b) 3D model and the finite element mesh of the thin structure.

An oscillatory displacement of $u_0 = sin\,2\pi t$ is applied at the ends of the structure as shown in figure 3.11(a), with the time being incremented from $t = 0$ to $t = 0.25s$ incrementally. The Green-Lagrange strain E_{11} of the deformed configuration is shown in figure 3.12(a). The elbow location of the serpentine structure undergoes the maximum strain in the x-direction. According to the spatial distribution of damage, shown in figure 3.12(b), the maximum damage is developed at the same location despite the boundary condition being applied at the ends. When a tension load is applied on the structure, both tension and compression deformation exist inside the structure. Since the damage can only initiate and evolve under tension, damage is suppressed when the local deformation is compressive.

The serpentine structure is analyzed by the ME-PE code, while also employing the damage indicator function in equation (3.68). Since damage mostly concentrates in the elbow region, the bottom surface with the coordinates $-2.0 \leq x \leq -1.6$, $0.18 \leq z \leq 0.22$ are analyzed. Figure 3.13(a) compares the results of the ME-PE simulation with the damage indicator function. The damage indicator function agrees with the simulation very well. The error between the two results in figure 3.13(b) is small and bounded.

3.A

The expression of ${}_tC^{Maxwell}_{IJKL}$ can be obtained from Eq. (3.27a) and Eq. (3.54c)

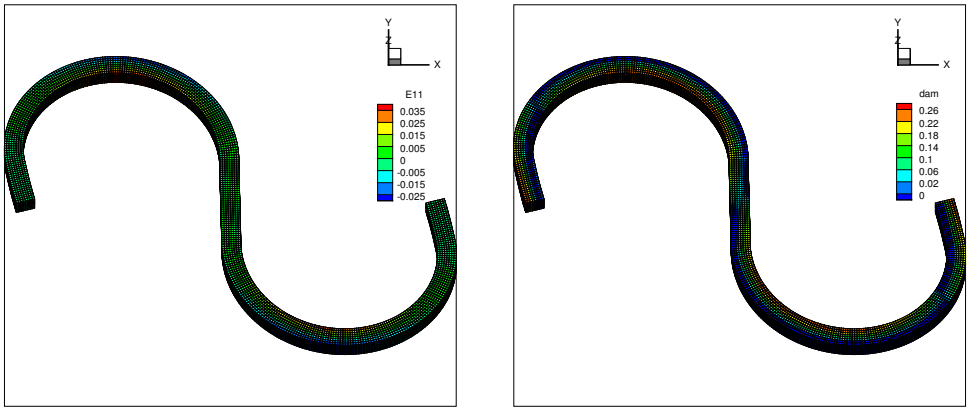

(a) (b)

Figure 3.12: (a) Green-Lagrange strain in the x-direction of the stretchable serpentine conductor, and (b) damage developed in the conductor with deformation.

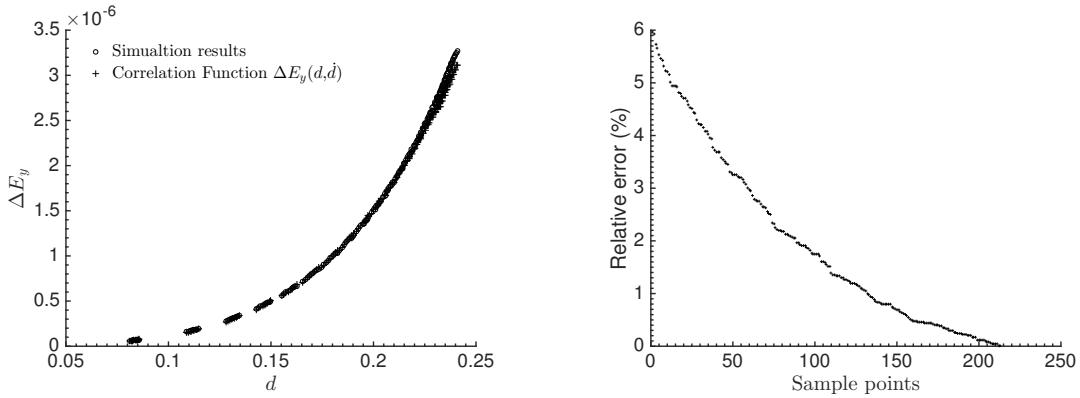

(a) (b)

Figure 3.13: (a) $\Delta E_y - D$ plot from the ME-PE code simulation and damage indicator function in equation (3.68), (b) relative error of the two results for the stretchable serpentine conductor.

$$
\begin{aligned}
{}_tC_{IJKL}^{Maxwell} = 2\frac{\partial S_{IJ}^{Maxwell}}{\partial C_{KL}} = -\frac{1}{2}\varepsilon E_P E_Q \Bigg[& \frac{J}{2} C_{KL} \left(C_{PQ}^{-1} C_{IJ}^{-1} - C_{PI}^{-1} C_{JQ}^{-1} - C_{PJ}^{-1} C_{IQ}^{-1} \right) \\
& + J C_{IJ}^{-1} \left(C^{-1} \odot C^{-1} \right)_{PQKL} + J C_{PQ}^{-1} \left(C^{-1} \odot C^{-1} \right)_{IJKL} \\
& - J C_{JQ}^{-1} \left(C^{-1} \odot C^{-1} \right)_{PIKL} - J C_{PI}^{-1} \left(C^{-1} \odot C^{-1} \right)_{JQKL} \\
& - J C_{IQ}^{-1} \left(C^{-1} \odot C^{-1} \right)_{PJKL} - J C_{PJ}^{-1} \left(C^{-1} \odot C^{-1} \right)_{IQKL} \Bigg]
\end{aligned}
\tag{3.69}
$$

where

$$
\left[(\bullet) \odot (\bullet) \right]_{IJKL} = \frac{1}{2} \left[(\bullet)_{IK} (\bullet)_{JL} + (\bullet)_{IL} (\bullet)_{JK} \right] \tag{3.70}
$$

The expression of $\mathscr{H}_{SIJ}^{Maxwell}$ is derived from Eq. (3.27a) and Eq. (3.55) as

$$
\mathscr{H}_{SIJ}^{Maxwell} = -\varepsilon J E_P \left[C_{PS}^{-1} C_{IJ}^{-1} - \left(C^{-1} \odot C^{-1} \right)_{PSIJ} \right] \tag{3.71}
$$

$$
\frac{\partial J}{\partial C_{IJ}} = \frac{J}{2} C_{IJ}^{-1} \tag{3.72}
$$

$$
\frac{\partial J^{-2/3}}{\partial C_{IJ}} = -\frac{1}{3} J^{-2/3} C_{IJ}^{-1} \tag{3.73}
$$

$$
\frac{\partial \overline{C}_{IJ}}{\partial C_{KL}} = \frac{\partial J^{-2/3}}{\partial C_{IJ}} = J^{-2/3} \left(\mathbb{I}_{IJKL} - \frac{1}{3} C_{IJ} \otimes C_{KL}^{-1} \right) \tag{3.74}
$$

Chapter 4

Conclusions

This report discusses major progress on three major tasks that have been conducted with this grant. They are summarized below.

4.1 Summary of Chapter 3

This chapter showcases the capabilities of a finite deformation cohesive zone enhanced phase-field model for simulating electromechanical fracture in heterogeneous piezocomposite microstructures with nonuniformly distributed inclusions. The stored electric energy density for the piezoelectric inclusions incorporates anisotropic elasticity of the material, along with the tension-compression split. The epoxy matrix is modeled as an isotropic Neo-Hookean material. Damage in the piezo-composite microstructure manifests in the form of interfacial decohesion at the inclusion-matrix interface with subsequent matrix cracking. Complex crack patterns and interactions among multiple cracks are very well captured by the phase-field model. Different electrical crack face conditions are incorporated and their effect on the evolution of electric field are illustrated. The example comparing the effect of the distribution of the fibers demonstrates the importance of taking into account the microstructural descriptors in upscaled damage models. Finally, the comparison of the electric field evolution in damaged and undamaged piezocomposite microstructures put forwards a novel concept of model-based approach of using piezocomposites as virtual damage sensors. The framework for this non-destructive in-situ damage sensing idea is being developed in ongoing research.

4.2 Summary of Chapter 4

This chapter develops a finite element model for multi-physics analysis, coupling transient electric and dynamic mechanical fields for a piezoelectric material. The model framework is able to predict the evolution of the electric field and its flux in a substrate undergoing finite deformation. Damage relations are implemented in the deformation model to account for change in mechanical and piezoelectric material properties with deformation induced damage evolution. To account for finite deformation and its effects on the electric field, a Lagrangian description is invoked to develop the finite element formulation. The piezoelectric material relation is implemented in the Lagrangian

description. Weak forms of the coupled transient piezoelectric and dynamic equations are generated in the reference configuration. The resulting finite element ME-PE code is parallelized using the ParMETIS library [22] for domain decomposition and the MPI-based PETSc library [3] for solving. The coupled mechanical-piezoelectric model with damage is validated and calibrated to serve as a electric field-based damage sensor.

The coupled mechanical-piezoelectric code is first validated by comparing with analytical results in the literature and with results from the commercial software ABAQUS for small deformation. An auxetic material is considered in the latter example with a convergence study for the coupled solver. Next a virtual damage sensor is proposed with the ME-PE code and simulation tool. A electric field-based damage indicator function is proposed and calibrated from data obtained through direction numerical solution using the ME-PE code. The function relates the electric field difference for undamaged and damaged conditions to the damage parameter D, its rate $\dot{D}$ and selected mechanical and piezoelectric material properties. The virtual damage sensor is used to examine damage conditions in a stretchable piezoelectric serpentine conductor. It has the potential to be a very effective tool for non-destructive evaluation of structures under dynamic loading conditions.

Bibliography

[1] ABAQUS. Dassault systems: Simulia, 2014.

[2] Amir Abdollahi and Irene Arias. Phase-field modeling of crack propagation in piezoelectric and ferroelectric materials with different electromechanical crack conditions. *J. Mech. Phys. Solids*, 60(12):2100–2126, 2012.

[3] Satish Balay, Jed Brown, , Kris Buschelman, Victor Eijkhout, William D. Gropp, Dinesh Kaushik, Matthew G. Knepley, Lois Curfman McInnes, Barry F. Smith, and Hong Zhang. PETSc users manual. Technical Report ANL-95/11 - Revision 3.4, Argonne National Laboratory, 2013.

[4] M Keith Ballard, W Ross McLendon, and John D Whitcomb. The influence of microstructure randomness on prediction of fiber properties in composites. *J. Compos. Mater.*, 48(29):3605–3620, 2014.

[5] Micheal Keith Ballard. Random fiber/matrix model generator, Jul 2017.

[6] Ivano Benedetti, Vincenzo Gulizzi, and Alberto Milazzo. A microstructural model for homogenisation and cracking of piezoelectric polycrystals. *Comput. Methods Appl. Mech. Eng.*, 357:112595, 2019.

[7] Tinh Quoc Bui, Sohichi Hirose, Chuanzeng Zhang, and et. al. Extended isogeometric analysis for dynamic fracture in multiphase piezoelectric/piezomagnetic composites. *Mech. Mater.*, 97:135–163, 2016.

[8] R. Bustamante, A. Dorfmann, and R.W. Ogden. On electric body forces and maxwell stresses in nonlinearly electroelastic solids. *Int. Jour. Engin. Sci.*, 47(11–12):1131 – 1141, 2009.

[9] M. G. Cain, M. Stewart, and M. Gee. Degradation of piezoelectric materials. Technical Report NPL Rep. SMMT (A) 148, National Physical Laboratory Management Ltd., Teddington, Middlesex, U.K., 1999.

[10] K.T. Chandrashekhara and A.N. Agarwal. Active vibration control of laminated composite plates using piezoelectric devices: a finite element approach. *Journal of Intelligent Material Systems and Structures*, 4(4):496–508, 1993.

[11] John D. Clayton. *Nonlinear mechanics of crystals*, volume 177. Springer Science & Business Media, 2010.

[12] E.F. Crawley and J. De Luis. Use of piezoelectric actuators as elements of intelligent structures. *AIAA Jour.*, 25(10):1373–1385, 1987.

[13] Saikat Dan, Preetam Tarafder, and Somnath Ghosh. Adaptive wavelet-enhanced cohesive zone phase-field fe model for crack evolution in piezoelectric composites. *Comput. Methods Appl. Mech. Eng.*, 392:114636, 2022.

[14] W Deng and SA Meguid. Closed form solutions for partially debonded circular inclusion in piezoelectric materials. *Acta Mech.*, 137(3):167–181, 1999.

[15] A. Erturk and D. J. Inman. An experimentally validated bimorph cantilever model for piezoelectric energy harvesting from base excitations. *Smart Mater. Struct.*, 18(2):025009, 2009.

[16] V Govorukha, M Kamlah, V Loboda, and Y Lapusta. Interface cracks in piezoelectric materials. *Smart Mater. Struct.*, 25(2):023001, 2016.

[17] Volodymyr Govorukha, Marc Kamlah, Volodymyr Loboda, and Yuri Lapusta. *Fracture mechanics of piezoelectric solids with interface cracks*. Springer, 2017.

[18] S. Guo and S. Ghosh. A finite element model for coupled 3d transient electromagnetic and structural dynamics problems. *Comp. Mech.*, 54(2):407–424, 2014.

[19] Q-C He and Q Shao. Closed-form coordinate-free decompositions of the two-dimensional strain and stress for modeling tension–compression dissymmetry. *J. Appl. Mech.*, 86(3):031007, 2019.

[20] R Jayendiran and A Arockiarajan. Theoretical modeling and experimental characterization of rate and temperature dependent electromechanical behavior of piezocomposites. *Eur. J. Mech. A. Solids*, 69:23–44, 2018.

[21] C. D. M. Junior, A. Erturk, and D. J. Inman. An electromechanical finite element model for piezoelectric energy harvester plates. *Jour. Sound Vib.*, 327(1-2):9–25, 2009.

[22] George Karypis, Kirk Schloegel, and Vipin Kumar. Parmetis parallel graph partitioning and sparse matrix ordering library version 3.1, August 2003.

[23] Sergii Kozinov, Meinhard Kuna, and Stephan Roth. A cohesive zone model for the electromechanical damage of piezoelectric/ferroelectric materials. *Smart Mater. Struct.*, 23(5):055024, 2014.

[24] M. Lax and D. F. Nelson. Maxwell equations in material form. *Physical Reviews B*, 13:1777–1784, 1976.

[25] C.K. Lee. Theory of laminated piezoelectric plates for the design of distributed sensors/actuators. Part i: Governing equations and reciprocal relationships. *Jour. Acoust. Soc. Amer.*, 87(3):1144–1158, 1990.

[26] L. Liu. An energy formulation of continuum magneto-electro-elasticity with applications. *Jour. Mech. Phys. Solids*, 63:451 – 480, 2014.

[27] Nanshu Lu and Shixuan Yang. Mechanics for stretchable sensors. *Curr. Opin. Solid State Mater. Sci.*, 19(3):149–159, 2015.

[28] Thirupathi Maloth and Somnath Ghosh. Coupled crystal plasticity phase-field model for ductile fracture in polycrystalline microstructures. *Submitted*, 2021.

[29] Tushar Kanti Mandal, Abhinav Gupta, Vinh Phu Nguyen, and et. al. A length scale insensitive phase field model for brittle fracture of hyperelastic solids. *Eng. Fract. Mech.*, 236:107196, 2020.

[30] Robert M McMeeking. The energy release rate for a griffith crack in a piezoelectric material. *Eng. Fract. Mech.*, 71(7-8):1149–1163, 2004.

[31] Robert M. McMeeking and Chad M. Landis. Electrostatic forces and stored energy for deformable dielectric materials. *Jour. Appl. Mech.*, 72(4):581, 2005.

[32] C. Miehe. Discontinuous and continuous damage evolution in ogden-type large-strain elastic materials. *Eur. Jour. Mech. A. Solids*, 14(5):697–720, 1995.

[33] C. Miehe, D. Rosato, and B. Kiefer. Variational principles in dissipative electro-magneto-mechanics: A framework for the macro-modeling of functional materials. *Int. Jour. Numer. Meth. Engin.*, 86(10):1225–1276, 2011.

[34] Christian Miehe, Martina Hofacker, and Fabian Welschinger. A phase field model for rate-independent crack propagation: Robust algorithmic implementation based on operator splits. *Comput. Methods Appl. Mech. Eng.*, 199(45-48):2765–2778, 2010.

[35] Christian Miehe, Fabian Welschinger, and Martina Hofacker. A phase field model of electromechanical fracture. *J. Mech. Phys. Solids*, 58(10):1716–1740, 2010.

[36] A. Mota and J. A. Zimmerman. A variational finite-deformation constitutive model for piezoelectric materials. *Int. Jour. Numer. Meth. Engin.*, 85(6):752–767, 2011.

[37] Thanh-Tung Nguyen, Julien Yvonnet, Danièle Waldmann, and Qi-Chang He. Implementation of a new strain split to model unilateral contact within the phase field method. *Int. J. Numer. Methods Eng.*, 121(21):4717–4733, 2020.

[38] Thanh-Tung Nguyen, Julien Yvonnet, Q-Z Zhu, Michel Bornert, and Camille Chateau. A phase-field method for computational modeling of interfacial damage interacting with crack propagation in realistic microstructures obtained by microtomography. *Comput. Methods Appl. Mech. Eng.*, 312:567–595, 2016.

[39] W. Nowacki. Foundations of linear piezoelectricity. In H. Parkus, editor, *Electromagnetic interactions in elastic solids*, volume 257, pages 105–157. Springer Verlag, Vienna, Austria, 1979.

[40] M. Okayasu, N. Odagiri, and M. Mizuno. Damage characteristics of lead zirconate titanate piezoelectric ceramic during cyclic loading. *Int. Jour. Fatigue*, 31(8):1434–1441, 2009.

[41] Y. H. Pao. Electromagnetic forces in deformable continua. *Mechanics today*, 4(7):1118–1126, 1978.

[42] Kyoungsoo Park, Glaucio H Paulino, and Jeffery R Roesler. A unified potential-based cohesive model of mixed-mode fracture. *J. Mech. Phys. Solids*, 57(6):891–908, 2009.

[43] Qing-Hua Qin and Yiu-Wing Mai. Crack path selection in piezoelectric bimaterials. *Compos. Struct.*, 47(1-4):519–524, 1999.

[44] Qing-Hua Qin and Yiu-Wing Mai. Crack branch in piezoelectric bimaterial system. *Int. J. Eng. Sci.*, 38(6):673–693, 2000.

[45] Qing-Hua Qin and Xi Zhang. Crack deflection at an interface between dissimilar piezoelectric materials. *Int. J. Fract.*, 102(4):355–370, 2000.

[46] Reinaldo Rodriguez-Ramos, Raul Guinovart-Diaz, Juan C Lopez-Realpozo, and et. al. Characterization of piezoelectric composites with mechanical and electrical imperfect contacts. *J. Compos. Mater.*, 50(12):1603–1625, 2016.

[47] J. A. Rogers, T. Someya, and Y. Huang. Materials and mechanics for stretchable electronics. *Science*, 327(5973):1603–1607, 2010.

[48] Y Sapsathiarn, T Senjuntichai, and RKND Rajapakse. Cylindrical interface cracks in 1-3 piezocomposites. *Composites, Part B*, 43(5):2257–2264, 2012.

[49] A. S. Semenov, H. Kessler, A. Liskowsky, and H. Balke. On a vector potential formulation for 3d electromechanical finite element analysis. *Commun. Numer. Methods Eng.*, 22(5):357–375, 2006.

[50] Ahmad Shahba and Somnath Ghosh. Coupled phase field finite element model for crack propagation in elastic polycrystalline microstructures. *Int. J. Fract.*, 219(1):31–64, 2019.

[51] Sicong Shan, Sung H Kang, Zhenhao Zhao, Lichen Fang, and Katia Bertoldi. Design of planar isotropic negative poisson's ratio structures. *Extreme Mechanics Letters*, 4:96–102, 2015.

[52] Kuldeep Sharma, Tinh Quoc Bui, Ch Zhang, and RR Bhargava. Analysis of a subinterface crack in piezoelectric bimaterials with the extended finite element method. *Eng. Fract. Mech.*, 104:114–139, 2013.

[53] J. C. Simo. On a fully three-dimensional finite-strain viscoelastic damage model: formulation and computational aspects. *Comp. Meth. Appl. Mech. Engin.*, 60(2):153–173, 1987.

[54] Jan G. Smits, Susan I. Dalke, and Thomas K. Cooney. The constituent equations of piezoelectric bimorphs. *Sensors Actuators A Phys.*, 28(1):41–61, 1991.

[55] A Sridhar and M-A Keip. A phase-field model for anisotropic brittle fracturing of piezoelectric ceramics. *Int. J. Fract.*, 220(2):221–242, 2019.

[56] Z Suo, C-M Kuo, DM Barnett, and JR Willis. Fracture mechanics for piezoelectric ceramics. *J. Mech. Phys. Solids*, 40(4):739–765, 1992.

[57] Z. Suo, X. Zhao, and W. H Greene. A nonlinear field theory of deformable dielectrics. *Jour. Mech. Phys. Solids*, 56(2):467–486, 2008.

[58] X. G. Tan and L. Vu-Quoc. Optimal solid shell element for large deformable composite structures with piezoelectric layers and active vibration control. *International Journal for Numerical Methods in Engineering*, 64(15):1981–2013, 2005.

[59] Shan Tang, Gang Zhang, Tian Fu Guo, and et. al. Phase field modeling of fracture in nonlinearly elastic solids via energy decomposition. *Comput. Methods Appl. Mech. Eng.*, 347:477–494, 2019.

[60] Preetam Tarafder, Saikat Dan, and Somnath Ghosh. Finite deformation cohesive zone phase field model for crack propagation in multi-phase microstructures. *Comput. Mech.*, 66(3):723–743, 2020.

[61] J.D. Thomas and N. Triantafyllidis. On electromagnetic forming processes in finitely strained solids: Theory and examples. *Jour. Mech. Phys. Solids*, 57(8):1391 – 1416, 2009.

[62] Carmine Trimarco. Material electromagnetic fields and material forces. *Arch. Appl. Mech.*, 77:177–184, 2007.

[63] Carmine Trimarco. On the dynamics of electromagnetic bodies. *Int. J. Adv. Eng. Sci. Appl. Math.*, 1:157–162, 2009.

[64] X Wang and Z Zhong. A conducting arc crack between a circular piezoelectric inclusion and an unbounded matrix. *Int. J. Solids Struct.*, 39(24):5895–5911, 2002.

[65] Zachary A Wilson, Michael J Borden, and Chad M Landis. A phase-field model for fracture in piezoelectric ceramics. *Int. J. Fract.*, 183(2):135–153, 2013.

[66] Jian-Ying Wu and Wan-Xin Chen. Phase-field modeling of electromechanical fracture in piezoelectric solids: Analytical results and numerical simulations. *Comput. Methods Appl. Mech. Eng.*, 387:114125, 2021.

[67] R. Yaghmaie and S. Ghosh. Computational modeling of finite deformation piezoelectric material behavior coupling transient electrical and mechanical fields. *Comp. Phys.*, 373:148–170, 2018.

[68] R. Yaghmaie, S. Guo, and S. Ghosh. Wavelet transformation induced multi-time scaling (watmus) model for coupled transient electro-magnetic and structural dynamics finite element analysis. *Comp. Meth. Appl. Mech. Engin.*, 303:341–373, 2016.

[69] X. H. Yang, C. Y. Chen, and Y. T. Hu. A static damage constitutive model for piezoelectric materials. In J. S. Yang and G. A. Maugin, editors, *Mechanics of Electromagnetic Solids*, pages 259–272. Springer US, Boston, MA, 2003.

[70] S. Yi, S. F. Ling, and M. Ying. Large deformation finite element analyses of composite structures integrated with piezoelectric sensors and actuators. *Fin. Elem. Anal. Design*, 35(1):1–15, 2000.

[71] Xiaofan Zhang, Daniel J O'Brien, and Somnath Ghosh. Parametrically homogenized continuum damage mechanics (phcdm) models for unidirectional composites with nonuniform microstructural distributions. *J. Comput. Phys.*, 435:110268, 2021.

[72] Xiaofan Zhang, Yanrong Xiao, Christopher S Meyer, and et. al. Impact damage modeling in woven composites with two-level parametrically-upscaled continuum damage mechanics models (pucdm). *Composites, Part B*, page 109607, 2022.

[73] X Zhao, H. Gao, G. Zhang, B. Ayhan, F. Yan, C. Kwan, and J. L Rose. Active health monitoring of an aircraft wing with embedded piezoelectric sensor/actuator network: I. Defect detection, localization and growth monitoring. *Smart Mater. Struct.*, 16(4):1208, 2007.